ÉCOLE POLYTECHNIQUE
FÉDÉRALE DE LAUSANNE

Simulation of the dynamics and transport of fast ions in the TORPEX turbulent plasma

Master project, Physics section
Automn semester 2008

Author: Alice Burckel

Supervisor: Professor A. Fasoli

Co-supervisor: Dr. P. Ricci

January 2009

Abstract

The simulation of the fast ions dynamics experiment in the TORPEX device is presented. The experiment consists of a fast particles source that injects lithium ions in the TORPEX plasma, characterized by interchange-driven turbulence. The simulations are performed by integrating the particles equations of motion in the turbulent fields provided by the simulations of Dr. Ricci et al. [15]. The accuracy of the integration of the eq. of motion has been established by testing the conservation of energy, and comparing the trajectories computed by the simulation with the predictions of the guiding center model. The study of a single particle motion has revealed chaotic behavior, and especially high sensitivity to the initial conditions. An approximation for the motion of the center of mass of a distribution of a statistically meaningful number of particles has been obtained for specific conditions. Finally the dependence of the spreading of the distribution on the fast particles energy, on the spreading in the initial velocities of the particles and on the spreading in the initial angles of the particles has been studied. It has revealed that the effects of turbulence on the spreading of a distribution are visible in the vertical and parallel directions as long as the spreading in the initial velocities is small (else, the effect of turbulence is masked by the effect of the magnetic field geometry) and in the radial direction for any values of the spreading in the initial velocities.

Acknowledgments

I would like to thank Paolo Ricci for his help and advises all along this project. I also thank the other member of the TORPEX group, in particular Christian Theiler, for their availability and their answers to my questions.

Contents

Introduction

The project ITER is the next big step in researches for using thermonuclear fusion as a new source of energy. While this experimental reactor is constructed, with the goal of demonstrating the scientific and technological feasibility of fusion energy for peaceful purposes (see ref. [9]), a very large effort from the international plasma physics community is provided in order to extrapolate, from the results of different tokamaks devices, basic plasma experiments and simulations, the physical understandings of the phenomena that will be faced in ITER.

A key difference between the plasma in present day devices and the plasma in ITER is the presence of energetic particles. Indeed, the D-T plasma in ITER will be self-heated by alpha particles (He-4), with energy of approximatively 3.5 MeV, that are produced by the fusion reactions. It is therefore fundamental to understand the interactions between these fast ions and the background plasma. Important researches are carried out about, on one hand, the fast ions dynamics (for example the creation of instabilities by interaction with Alfvén modes or the accumulation of fast ions into 'helium ashes' that could slow down the fusion reactions), and, on the other hand, the interactions between fast ions and existing instabilities. An area of research is the interaction between fast ions and low-frequency plasma turbulence. The CRPP is currently building an experiment on this specific topic that consists in injecting fast ions of Lithium, with energy between 100 eV - 1 keV, in a plasma experimenting low frequency turbulence driven by drift and interchange instabilities. An experiment of this kind cannot be realized in a tokamak, where the temperature is too high to insert fast ions probe and source. It is therefore realized on the device TORPEX (TOroidal Plasma EXperiment) dedicated to basic plasma experiments, where the plasma temperature of about 5 eV allows the insertion of a small source inside the vacuum vessel.

The goal of the project presented here is to realize a simulation of this experiment; i.e to simulate the evolution of a distribution of fast ions of Lithium in a potential created by interchange instabilities (the drift instabilities are not taken into account in this simulation). This work is a continuation of the project started last term as a "Travaux pratiques 4" project, where the motion of a single particle in a stable magnetic field has been implemented, two different methods for solving the equations of motion has been tested and the effect of a very simple electric field on the motion of a single particle has been studied. During the project presented here, the motion of a single particle in a potential simulating the interchange instabilities has been implemented and tested, and then the motion of a statistically meaningful number of particles has been studied. The accent has been put on the effects of the turbulence on the ions dynamics; especially the effects on the center of mass of the distribution, and on the spreading of the ions, both in the directions parallel and perpendicular to the magnetic field lines.

This report starts with a description of the TORPEX device and of the fast ions experiment currently built, followed by a review of some elements of theory used in the project. The second chapter describes the important characteristics of the simulation, and the different tests that have been performed. The third chapter presents the study of a single particle motion. Finally, the last chapter presents the results obtained for a distribution of particles. This last chapter is divided into two distinct studies: the study of the motion of the center of mass of the distribution, and the analysis of the spreading of the distribution. As often as possible, some links are established between the present results, and what will be observable in the real experiment.

Chapter 1

Theoretical and experimental background

This chapter starts with a description of the TORPEX device, and the fast ion experiment currently built on TORPEX. Then, it gives a summary of the elements of theory used to study the particles motion. This second part presents the guiding center model, used to give an approximation of the trajectories of the particles, a description of the interchange instabilities responsible for the plasma turbulence studied in this project, and finally presents some basic elements of the theory of transport in plasmas.

1.1 The experiment

1.1.1 The TORPEX device

TORPEX is a toroidal plasma machine dedicated to basic plasma experiments. The radius of the torus is 1m and the radius of its poloidal section is 0.2m. In TORPEX, the plasma is submitted to a toroidal magnetic field B_Φ of about 0.1T and a vertical magnetic field B_z of about $5 \cdot 10^{-3}$T. The plasma is confined in the poloidal plane, but, since the magnetic field lines are open, there are plasma losses at the walls of the machine. For this reason, the production of plasma is ensured by the ionization of neutral gas continuously injected. The duration of the plasma discharges can be up to 1.8 s [12]. The four gases that are typically used to form plasma in TORPEX are Hydrogen, Helium, Neon and Argon. The typical values of electron temperature and density are $T_e = 5eV$ and $n_e = 10^{16}m^{-3}$ (i.e. much smaller than in most of the tokamaks). The pressure in the machine depends on the type of plasma, but varies between 10^{-5} mbar and 10^{-4} mbar [5]. The plasma in TORPEX are subject to interchange instabilities and drift instabilities.

1.1.2 The fast ion experiment

In the fast ions experiment on TORPEX, ions of Lithium will be injected in the plasma, in order to study the interactions between fast ions and low-frequency plasma turbulence. Light ions are used, because their high velocity facilitates the fast ion-

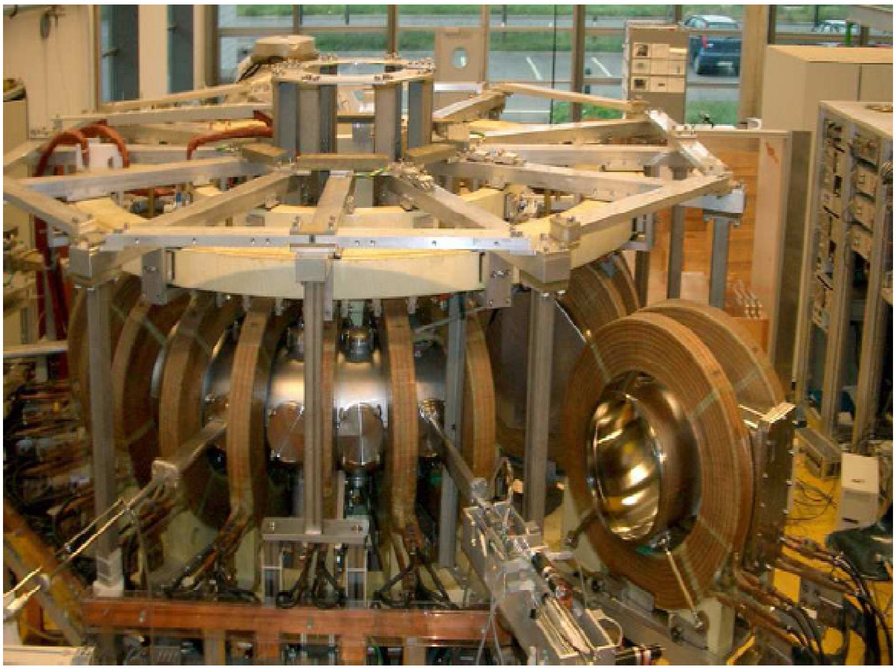

Figure 1.1: View of TORPEX. Picture coming [5]

electron interactions [12]. The source is an aluminosilicate Li-6 ion emitter. It is cylindrical with a length of about 4 cm and can be installed inside the vacuum vessel. The energy of the fast ions, as well as the focus of the beam are adjustable. The fast ions should have an energy much higher than the plasma temperature, but low enough to be confined by the toroidal magnetic field. The energies that satisfy these conditions are included in the interval between 100eV and 1keV [12].

The detector is a gridded energy analyzer that can measure the location, energy, and current density profile of the ion beam[12]. The source and the detector can cover almost the entire poloidal cross section thanks to a two-dimensional poloidally moving system allows

1.2 The guiding center

When a charged particle moves in a magnetic field, its motion can be decomposed in the high frequency rotation perpendicular to the magnetic field lines called the Larmor rotation, and the slower motion of the center of the Larmor rotation. This center of the Larmor rotation is called the guiding center of the trajectory, and moves along the magnetic field lines with eventually a perpendicular drift. The motion of the guiding center depends on:

1. The electric field

2. The gradient of the magnetic field

3. The curvature of the magnetic field

An analytical calculation of this motion as been performed in ref. [6]. However, the equations obtained for the motion of the guiding center are only valid under the assumption that the electromagnetic potential does not vary much, on the area of a Larmor rotation. This is satisfied when the variation of potential is small (so the electric field is small), and when the Larmor radius is small. This gives the two first conditions for the application of the guiding center model [6]:

- Small variation of the electric field:

  $$\frac{cE}{vB} << 1 \tag{1.1}$$

  In this simulation, this condition is satisfied for all the possible initial velocities. Indeed, when T=100 eV (smallest value of the energy considered), this ratio is equal to about 0.13.

- Small Larmor radius compared to the length of variation of the potential. We define $l \simeq |\bigtriangledown ln(\phi)|^{-1}$ as the scale length for changes in macroscopic parameters and $\lambda_L = \frac{v_\perp mc}{qB}$ as the ion Larmor radius. The condition is:

  $$\delta = \frac{\lambda_L}{l} << 1 \tag{1.2}$$

  In the potential considered for this project, $l \sim$ 5cm. Therefore, the Larmor radius, which depends on the initial energy of the particle and on the angle of inclination of the source compared to the magnetic field lines, has to be much smaller than 5cm. This is not respected, for example, in a simulation at T=1 keV (highest value of the energy considered), because there, $\lambda_L \sim$ 4cm when the source is parallel to the magnetic field lines, and goes up to $\lambda_L \geq$ 6cm when the source is at 45 degrees.

The theory gives a third condition for the application of the guiding center model on the variation of $\phi(t)$ in time [6]:

- $$\frac{\partial ln(\phi(t))}{\partial t} = O(\delta^2 \omega) \tag{1.3}$$

  where $w = v/l$ is the transit frequency.

Let's define $\hat{b} = \frac{\vec{B}}{|\vec{B}|}$ as the unit vector parallel to the magnetic field lines and $\Omega = \frac{qB}{mc}$ as the ion cyclotronic frequency. $\vec{E}$ and $\vec{B}$ are the fields felt by the particle at a given time t, and $v_\perp$ and $v_\parallel$ are the decomposition of the particle velocity $\vec{v}$ at time t. The velocity of the guiding center of the particle at time t is given by the following equation [6]:

$$\vec{v_{gc}} = (v_\parallel + \hat{v_\parallel})\hat{b} + \vec{v_D} \tag{1.4}$$

where

$$\hat{v_\parallel} = (\frac{v_\perp^2}{2\Omega})\hat{b}\cdot\vec{\nabla}\times\hat{b} \tag{1.5}$$

$$\vec{v_D} = \frac{c\vec{E}\times\hat{b}}{B} + \hat{b}\times\frac{(\frac{v_\perp^2}{2B}\vec{\nabla}B + v_\parallel^2\hat{b}\cdot\vec{\nabla}\hat{b} + v_\parallel\frac{\partial\hat{b}}{\partial t})}{\Omega} \tag{1.6}$$

The velocity of the guiding center is decomposed in a term in the direction parallel to the magnetic field lines (equal to the parallel velocity of the particle and a parallel drift $\hat{v_\parallel}$) and in a drift in the perpendicular plane $\vec{v_D}$. In our geometry, $\vec{\nabla}\times\hat{b} = 0$. Therefore, the parallel drift is always equal to 0. This implies that the parallel velocity of the guiding center is conserved.

Moreover, $\hat{b}$ is independent of time, so $\frac{\partial\hat{b}}{\partial t} = 0$. It follows that:

$$\vec{v_D} = \overbrace{\frac{c\vec{E}\times\hat{b}}{B}}^{=\vec{v}_{\vec{E}\times\vec{B}}} + \hat{b}\times\frac{(\frac{v_\perp^2}{2B}\vec{\nabla}B + v_\parallel^2\hat{b}\cdot\vec{\nabla}\hat{b})}{\Omega} \tag{1.7}$$

$$\tag{1.8}$$

The first term is called the $\vec{E}\times\vec{B}$-drift, and acts in the plane perpendicular to the magnetic field lines. The second term contains the effect on the inhomogeneity of $\vec{B}$, and the curvature. In the geometry of this experiment, this second term acts only in the vertical direction (corresponding to the vertical unit vector $\hat{e_z}$), and, after some calculations, the velocity of the guiding center can finally be expressed as:

$$\vec{v_{gc}} = v_\parallel\hat{b} + \vec{v}_{\vec{E}\times\vec{B}} + \frac{1}{r}(\frac{v_\perp^2}{2} + v_\parallel^2)\frac{\hat{e_z}}{\Omega} \tag{1.9}$$

In the present study, the motion of the particles obtained by numerical resolution of differential equations will often be compared with the equations of their guiding centers.

1.3 The interchange instability

Magnetized plasmas are prone to various instabilities, induced both by the fluid and the electromagnetic characteristics of the plasma. In this experiment, the fast ions are moving through a plasma dominated by drift and interchange instabilities. However, in this simulation, only turbulence driven by the interchange instabilities are considered.

The interchange instability can easily be understood when it is compared with its analogous in fluid mechanics: the Rayleigh-Taylor instability that is triggered, for example, when two fluids are submitted to a strong external field, like gravity, and the heavier fluid is supported by the lighter one. The two fluids are at an unstable equilibrium. As soon as the interface is perturbed, the system decreases its potential energy by letting the two fluids blend. The viscosity induces non-linear effects that create bubbles and local convective cells.

For the interchange instability, the plasma can be described as a fluid. In the presence of an important gradient of density, the plasma can be divided in two zones of different density. Similarly to the Rayleigh-Taylor case, the interchange instability appears at the interface between these two zones. However, in the plasma, the dominant external field is not gravity, but the effect of the curvature and the inhomogeneity of the magnetic field. Figure 1.2 illustrates the development of the interchange instability. First, the interface is at equilibrium. Then, a perturbation generates some local separations of charges at the interface. This induces the creation of a local electric field. Due to the presence of an electric field and the external magnetic field, an $\vec{E} \times \vec{B}$-drift appears, that amplifies the perturbations, leading to non-linear effects and the formation of bubbles. Some of the high-density bubbles, called 'blobs', are then free to move in the low density region of the plasma.

Since the $\vec{E} \times \vec{B}$-drift is in the plane perpendicular to the magnetic field lines, the interchange instabilities growth only in this plane and not in the direction parallel to $\vec{B}$ (i.e. $K_{\|} = 0$).

The growth rate of the interchange instabilities is given by [13]:

$$\gamma = \frac{\sqrt{2}\, c_s}{\sqrt{(R\, L_p)}} \tag{1.10}$$

Where $c_s = \frac{T_e}{m_i}$ is the speed of sound, R is the major radius of the machine, and $L_p = |(\frac{1}{p}\frac{dp}{dr})^{-1}|$ is the caracterisitc length of the equilibrium pressure.

1.4 Transport in plasmas

The main objective of this project is to characterize the dynamics and transport of fast ions of Lithium in a turbulent plasma. The mostly common theory used to describe the dynamics of an ensemble of particles is the anisotropic 3D diffusion equation:

$$\frac{\partial P(\vec{x},t)}{\partial t} = \sum_{i=1}^{3}\sum_{j=1}^{3} \frac{\partial}{\partial x_i}(D_{ij}(P,\vec{x})\frac{\partial P(\vec{x},t)}{\partial x_j}) \tag{1.11}$$

Where D is a symmetric positive definite matrix of the diffusion coefficients. If the diffusion is isotropic and D is constant, the above equation reduces to:

$$\frac{\partial P(\vec{x},t)}{\partial t} = D \bigtriangledown^2 P(\vec{x},t) \tag{1.12}$$

However, in the study of transport in fusion plasmas, it appears that, in many situations [3] the transport is non-diffusive; i.e Eq.(1.9) is not satisfied by the ensemble of particles. A simple diagnostic to reveal non-diffusive transport is the scaling of the second moment of particles displacements [4], $\sigma^2(t) =< [\delta y(t) - < \delta y(t) >]^2 >$ where $< >$ is an ensemble average over a large distribution of particles. Assuming that its behavior follows the general law:

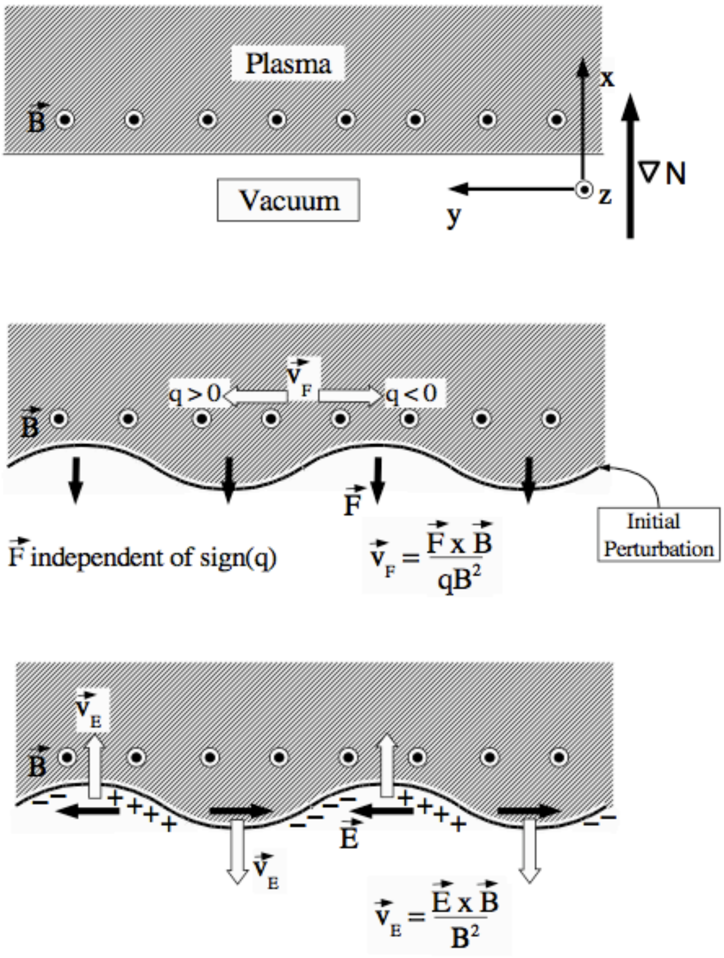

Figure 1.2: Figures extracted from [2] that presents the development of the interchange instability, in a magnetized plasma with density gradient and submitted to an external force $\vec{F}$ perpendicular to $\vec{B}$. 1) The system is at equilibrium. 2) The force $\vec{F}$ generates a perturbation that leads to a separation of charges and the apparition of an electric field. 3) The $\vec{E} \times \vec{B}$-drift amplifies the perturbation, which generates instabilities.

$$\sigma^2(t) \sim t^\gamma \tag{1.13}$$

in the case of standard diffusion, $\gamma = 1$, and an effective diffusivity coefficient can be defined as $D_{eff} = lim_{t\to\infty}\frac{\sigma^2(t)}{2t}$. In the case of non-diffusive transport, $\gamma \neq 1$. If $0<\gamma<1$, the transport is called sub-diffusive, and the spreading is slower than in standard diffusion. If $1<\gamma<2$, the transport is called super-diffusive. For non-diffusive transport, it is not relevant to study the 'effective diffusivity' since, following the previous definition, D_{eff} is either equal to 0 or equal to ∞. When $\gamma=2$, the transport is called ballisitic spreading, it corresponds to the simple case $\sigma \sim t$. The physical meaning of the ballistic spreading is that the average relative velocities of the particles do not depend on time. Indeed, by definition:

$$\begin{aligned} \sigma^2 &= \frac{1}{N}\sum_{i=1}^{N}(\delta y_i(t) - < \delta y_i(t) >)^2 && (1.14)\\ &= \frac{1}{N}\sum_{i=1}^{N}(v_{y_i}(t)\cdot t - < v_{y_i}(t) > \cdot t)^2 && (1.15)\\ &= \frac{t^2}{N}\sum_{i=1}^{N}\underbrace{(v_{y_i}(t) - < v_{y_i}(t) >)^2}_{U} && (1.16) \end{aligned}$$

and $\gamma=2$ is only satisfied when the term U=0.

Another diagnostic of non-diffusive transport is the study of the probability distribution function (PDF) of particle displacements [4]. Numerically, P(t) is the normalized histogram of the particle positions at time t. In the case of diffusive transport, the central limit theorem implies that P tends to a gaussian distribution that satisfy diffusive scaling [4]:

$$P_G = t^{-1/2}G([\delta y(t) - < \delta y(t) >]/t^{1/2}) \tag{1.17}$$

where G is a Gaussian. In the non-diffusive case, P follows a more general form of scaling:

$$P = t^{-\gamma/2}L([\delta y(t) - < \delta y(t) >]/t^{\gamma/2}) \tag{1.18}$$

where L is a general non-gaussian function, and γ is the same exponent than the one given by equation 1.13. Thus, it can be shown that P is invariant with respect to the space-time renormalization transformation [4]:

$$([\delta y(t) - < \delta y(t) >], t) \rightarrow (\lambda^{\gamma/2}\,[\delta y(t) - < \delta y(t) >], \lambda t) \tag{1.19}$$

where λ is a scale factor. This fact will be used to test the accuracy of the values of the γ's found with the analysis of the second moment of the particle displacements. Indeed, if the exponents are correct, then plots of $t^{\gamma/2}\,P$ vs $[\delta y(t) - < \delta y(t) >]/t^{\gamma/2}$ for different time t would all collapse into the same function L [4].

The observation of non-diffusive transport has created a need for models capable of describing these non-diffusive phenomena. A possible approach is to generalize the diffusion equation by using fractional derivatives [3]. Even if this model has not been used in this project, it is briefly presented because it gives an outlook of the possible studies that could be realized beyond this project. The generalized spatial fractional derivative of order α (where n-1< α<n, and n is an interger), at position x (x is contained in the interval [a,b], the most general case being $a = -\infty$ and $b = \infty$), is defined as [3]:

$$D_x^{\alpha} f = [l_a D_x^{\alpha} + r_x D_b^{\alpha}] f \tag{1.20}$$

where ${}_aD_x^{\alpha} f$and ${}_xD_b^{\alpha} f$ are respectively the left and right fractional derivatives defined as:

$$\begin{aligned} {}_aD_x^{\alpha} f &= \frac{1}{\Gamma(n-\alpha)} \frac{\partial^n}{\partial x^n} \int_a^x \frac{f(u)}{(x-u)^{\alpha-n+1}} du & (1.21) \\ {}_xD_b^{\alpha} f &= \frac{(-1)^n}{\Gamma(n-\alpha)} \frac{\partial^n}{\partial x^n} \int_x^b \frac{f(u)}{(u-x)^{\alpha-n+1}} du & (1.22) \end{aligned}$$

and r and l are weighting factors. When α is an integer, they correspond to the standard derivatives.

Similarly, the generalization of the time derivative $\frac{\partial}{\partial t}$is the temporal fractional derivative of oder β, that can be defined as [3]:

$$D_t^{\beta} f = \frac{1}{\Gamma(1-\beta)} \int_0^t \frac{\partial_{\tau} f(\tau)}{(t-\tau)^{\beta}} d\tau \tag{1.23}$$

The generalized fractional diffusion equation proposed in this approach becomes:

$$D_t^{\beta} P = \chi D_x^{\alpha} P \tag{1.24}$$

Where α and β characterize the transport. When $\alpha = 2$ and $\beta = 1$, Eq.(1.24) corresponds to the standard diffusion equation. Furthermore, in this model, α and β are related to the exponent γ, given by equation 1.13, through [4]:

$$\gamma = \frac{2\beta}{\alpha} \tag{1.25}$$

The fractional diffusion model reproduces non-diffusive phenomenology [3] .

Chapter 2

Building the simulation

This chapter starts with the presentation of the geometry chosen for the simulation. Then it details the approximations made for the magnetic and the electric fields in which the fast particles will move, the method chosen to solve the equations of motion and the values of the principles parameters of the simulation. After that, it presents the main tests that have been performed in order to prove the physical validity of the simulation. Finally, it ends with a description of the implementation of the motion of a distribution of particles.

2.1 Description of the simulation

2.1.1 Geometry of the experiment

In the simulation, TORPEX is viewed as a toroidal vaccuum vessel with absorbing walls. The main approximation made about its geometry is to replace the circular poloidal section by a rectangle of 40cm x 40cm.

Coordinate systems

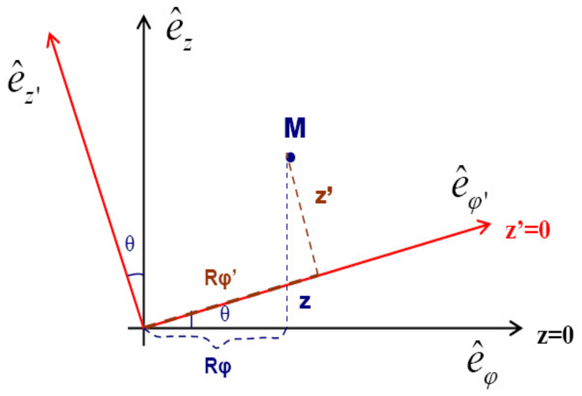

Figure 2.1: Change of coordinates in the plane perpendicular to the field lines

The equations of motion are solved in a cartesian coordinates system. However, the coordinate system that is the most natural to describe the geometry of TORPEX is the cylindrical coordinates $(\hat{e_r}, \hat{e_\varphi}, \hat{e_z})$. Moreover, since the magnetic field $\vec{B}$ has a toroidal component B_{th}, and a vertical component B_v, the magnetic field lines are tilted up by an angle $\theta = atan(\frac{B_z}{B_{th}})$. Therefore, it is physically meaningful to express the results in a geometry that separates the direction parallel to the field lines, and the plane perpendicular to it. For this reason, all the data analysis will be performed in the coordinate system $(\hat{e_r}, \hat{e_{\varphi'}}, \hat{e_{z'}})$, where $\hat{e_{\varphi'}}$ is the unit vector parallel to the magnetic field lines. Figure 2.1 presents the definition of this new coordinates for a generic point M. The generic point M can be expressed in the different coordinate systems:

$$\begin{aligned} M &= r\hat{e_r} + r\varphi\hat{e_\varphi} + z\hat{e_z} & (2.1) \\ &= r\hat{e_r} + r\varphi'\hat{e_{\varphi'}} + z'\hat{e_{z'}} & (2.2) \end{aligned}$$

The two coordinate systems are linked through the standard equations for a rotation:

$$\begin{aligned} \hat{e_{\varphi'}} &= \cos(\theta)\hat{e_\varphi} + \sin(\theta)\hat{e_z} & (2.3) \\ \hat{e_{z'}} &= -\sin(\theta)\hat{e_\varphi} + \cos(\theta)\hat{e_z} & (2.4) \end{aligned}$$

From there, it follows that:

$$\begin{aligned} z = r\varphi'\sin(\theta) + \cos(\theta)z' \qquad & r\varphi' = \cos(\theta)r\varphi + \sin(\theta)z & (2.5) \\ r\varphi = r\varphi'\cos(\theta) - z'\sin(\theta) \qquad & z' = z\cos(\theta) - r\varphi\sin(\theta) & (2.6) \end{aligned}$$

We note that the angle of inclination of $\hat{e_{\varphi'}}$, θ, depends on B_{th}. Since B_{th} is inversely proportional to r, θ also depends on r. However, in the present work, this dependence is neglected, and we assume $\theta = \theta(r = R)$. With this assumption, every potential $\phi = \phi(r, z')$ provides a conservative electric field.

In this report, the angle θ refers always to the inclination of the magnetic field lines $\theta(r = R) = atan(\frac{B_z}{B_{th}(r=R)})$ and the plane formed by the vectors $(\hat{e_r}, \hat{e_{z'}})$ is often refered as 'the tilted plane'.

2.1.2 Equations of motion

The fast ions injected in the plasma interact with the magnetic field and the turbulent electric field created by the plasma itself. In this simulation, the collisions between fast ions and plasma particles or neutrals are not taken into account. Thus, the equations of motion that describe the trajectory of one ion are:

$$\begin{cases} \frac{d\vec{r}}{dt} = \vec{v} \\ m\frac{d\vec{v}}{dt} = q(\vec{E}(\vec{r}, t) + \vec{v} \times \vec{B}(\vec{r}, t)) \end{cases} \qquad (2.7)$$

where m and q are the mass and charge of the ion, $\vec{r}$ and $\vec{v}$ are its position and velocity, and $\vec{E}(\vec{r}, t)$ and $\vec{B}(\vec{r}, t))$ are the electric field and magnetic field felt by the ion at time t. The calculation of these fields is explained below.

It has been chosen to integrate the full equations of motion and not only the equations of the guiding center of each particle, because it has been observed, that in certain cases, the guiding center assumptions are not respected.

Magnetic field

The magnetic field in the experiment is created by 28 coils. For this reason, the field depends on the poloidal cross-section. Indeed, it is more intense in a poloidal cross-section near a coil than in one between two coils. However, this effect is neglected in the simulation, and $\vec{B}$ is chosen to be independent of the poloidal cross-section. $\vec{B}$ (expressed in cylindrical coordinates) has a toroidal and a vertical component:

$$\vec{B} = B_0 \frac{R}{r} \hat{e_\varphi} + B_z \hat{e_z} \tag{2.8}$$

Where R=1m is the normalization constant (that is equal, in this geometry, to the center of the poloidal section). In cartesian coordinates this leads to

$$\begin{aligned} \vec{B} &= -B_0 \frac{R}{r} \sin(\varphi) \hat{e_x} + B_0 \frac{R}{r} \cos(\varphi) \hat{e_y} + B_z \hat{e_z} & (2.9) \\ &= -B_0 \frac{Ry}{r^2} \hat{e_x} + B_0 \frac{Rx}{r^2} \hat{e_y} + B_z \hat{e_z} & (2.10) \end{aligned}$$

We define dB as $dB = \frac{B_z}{B_0}$, and $A = \frac{R}{r^2}$. The decomposition of the magnetic field on cartesian coordinates becomes:

$$\vec{B} = B_0 \begin{pmatrix} -Ay \\ Ax \\ dB \end{pmatrix} \tag{2.11}$$

The ratio of $dB = \frac{B_z}{B_0}$ is chosen to be equal to 0.0224, corresponding to a vertical magnetic field B_z of about 0.002 T.

Electric field

In this simulation, the fast particles move through a turbulent plasma. This plasma has been simulated by Dr. Ricci et al. in November 2007 [15]. The simulations provide the values of the electromagnetic potential $\phi(\vec{x}, t)$. And from this, the electric field that affects the particle motion can be found. The plasma is a plasma of hydrogen, with a mean electron temperature of $T_e = 3.5eV$, and a mean electron density of about $1 \cdot 10^{16} m^{-3}$. The mean pressure is $4 \cdot 10^{16} Pa$. In this simulation, the ions are frozen. This type of plasma is subject to the interchange instabilities (see section 1.2).

In the simulation of ref. [15], measurements have been taken every 2.7μs. At each measurement is saved a grid of 256x64 values of the electromagnetic potential $\phi(\vec{x}, t)$. This grid is in the plane perpendicular to the magnetic field lines ('tilted plane'). The length of it is 0.4m radially (with corresponds to the size of the vacuum vessel), and its height (Δ) is the distance between the return of one field line on the tilted plane, which is equal, in this simulation, to 0.14m. The simulated potential experiences only turbulence driven by interchange instabilities. Since, for these instabilities, $K_\parallel = 0$, the system is invariant under a rotation of $\varphi' = 2\pi$. Therefore, the potential is periodic in the z'-direction with a period of Δ. Figure 2.2 shows one grid of this potential.

By differentiating this $\phi(\vec{x}, t)$ along r and along z', one can obtain two grids of E_r and $E_{z'}$. Thus, the values of the electric field are only known on the 256x64 points of the grid. It will be shown in section 2.2 that, to obtain the values of $\vec{E}$ at a generic point, it is not possible to simply use a linear interpolation of the values at each corner of the grid square that contains the point. Indeed, this solution give an electric field that does not conserve energy. An appropriate way of solving this problem is to use the bicubic interpolation method (see Appendix A.1 and ref. [13]).

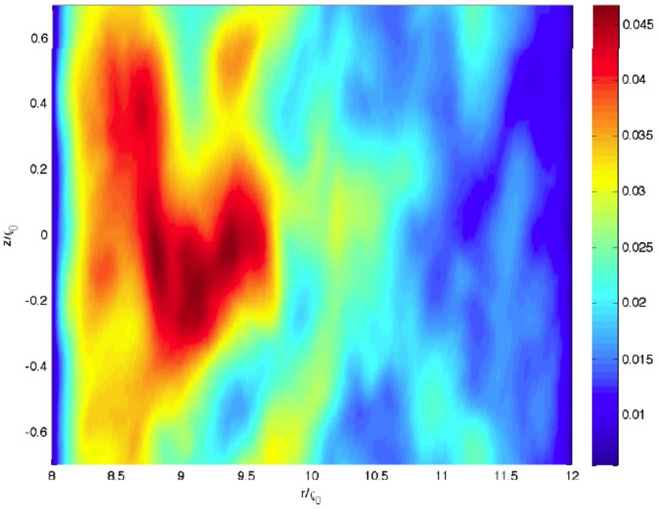

Figure 2.2: simulated potential between the return of the same magnetic field line on the tilted plane.

Another thing that needs to be taken into account is the fact that, physically, $\vec{E}$ varies continuouly with time. But the simulations only give the values of $\vec{E}$ every 2.7μs. In will be shown in section 2.2, that, to obtain the value of $\vec{E}(\vec{x}, t)$ on a generic point, at a given time t, it is possible to take a linear interpolation between the values of $\vec{E}(\vec{x})$ on the two grids which correspond to the two measurements before and after t.

Mathematically, the derivation of $\vec{E}$ from the potential, in the plane perpendicular to the magnetic field lines, follows (equations given in the $(\hat{e_r}, \hat{e_{\varphi'}}, \hat{e_{z'}})$ coordinates system):

$$\vec{E}(\vec{x}, t) = -\vec{\bigtriangledown}\phi(\vec{x}, t) = -\begin{pmatrix} \frac{\partial}{\partial r}\phi(\vec{x}, t) \\ \frac{1}{r}\frac{\partial}{\partial \varphi'}\phi(\vec{x}, t) \\ \frac{\partial}{\partial z'}\phi(\vec{x}, t) \end{pmatrix} = \begin{pmatrix} -\frac{\partial\phi(\vec{x},t)}{\partial r} \\ 0 \\ -\frac{\partial\phi(\vec{x},t)}{\partial z'} \end{pmatrix} \tag{2.12}$$

where $-\frac{\partial\phi(\vec{x},t)}{\partial r}$ and $-\frac{\partial\phi(\vec{x},t)}{\partial z'}$ are obtained as explained above. This can be then transformed in cartesian coordinates through:

$$\vec{E} = -(\frac{\partial\phi(\vec{x},t)}{\partial r}) \begin{pmatrix} \frac{x}{r} \\ \frac{y}{r} \\ 0 \end{pmatrix} + (-\frac{\partial\phi(\vec{x},t)}{\partial z'}) \begin{pmatrix} \frac{y}{r}\, sin(\theta) \\ -\frac{x}{r}\, sin(\theta) \\ cos(\theta) \end{pmatrix} \tag{2.13}$$

2.1.3 Normalized units

In the simulation, it is easier to solve the equations of motion using adimensionalised units. The normalization chosen can be summarized by the following equations that relate the adimensional quantities, $\tilde{t}$, $\tilde{\vec{r}}$, $\tilde{T}$, $\tilde{\vec{B}}$ and $\tilde{m}$ to the physical quantities t, $\vec{r}$, T, $\vec{B}$ and m:

$$t = \Omega^{-1}\tilde{t} \tag{2.14}$$

$$T = T_0\tilde{T} \tag{2.15}$$

$$\vec{r} = \lambda_L\tilde{\vec{r}} \tag{2.16}$$

$$\vec{B} = B_0\tilde{\vec{B}} \tag{2.17}$$

$$m = m_0\tilde{m} \tag{2.18}$$

Where $\Omega = \frac{qB_0}{m_0}$ is the ion cyclotronic frequency and $\lambda_L = \frac{\sqrt{T_0}}{\Omega}$ is the ion Larmor radius. It has been chosen for the normalization T_0=1 KeV, $B_0 = 0.076$ T and $m_0 = 6 \cdot 1.67 \cdot 10^{-27}$ Kg, the mass of the Lithium ion. It follows that $\lambda_L = 0.1$m and $\Omega = 1.21 \cdot 10^6$Hz.

Table 2.1 presents the values chosen for the typical parameters of a simulation in normalized units, and also how to convert them back to physical units.

parameter	[norm. unit]	[phys. unit]
Vertical magnetic field	$\tilde{B}_z = 0.0224$	$B_z = \tilde{B}_z \cdot B_0 = 0.0017$ T
Initial energy of the ion	$\tilde{T} = 0.1$	$T_0 = \tilde{T} \cdot T_0 = 100$ eV
Initial position	$\tilde{x}_i = 10$	$x_i = \tilde{x}_i \cdot \lambda_L = 1.0$ m
Time of the simulation	$\tilde{D} = 700$	$D = \tilde{D}/\Omega = 5.79 \cdot 10^{-4}$s
Increment of time	$\tilde{\Delta t} = 0.01$	$\Delta t = \tilde{\Delta t}/\Omega = 8.3$ ns

Table 2.1: Typical values chosen for the main parameters of the simulation, given in normalized units and in real units.

The normalization of the energy of a particle gives:

$$\epsilon = \frac{v^2}{2} + e\frac{\phi}{m} \overset{\text{n.u.}}{\overbrace{=}} v_0^2 \underbrace{[\frac{\tilde{v}^2}{2} + \tilde{\phi}]}_{\tilde{\epsilon}} \tag{2.19}$$

With these normalized units, the equations of motion become simply:

$$\begin{cases} \frac{d\tilde{\vec{r}}}{d\tilde{t}} = \tilde{\vec{v}} \\ \frac{d\tilde{\vec{v}}}{d\tilde{t}} = \tilde{\vec{v}} \times \tilde{\vec{B}}(\tilde{\vec{r}}, t) \end{cases} \tag{2.20}$$

In order to simplify the notation, all the symbols $\sim$ have been dropped in the following.

2.1.4 Method for solving the equations

The main idea to solve numerically the equations of motion is to discretize them and find an algorithm that gives, at each step, the values of the quantites $\vec{r}$ and $\vec{v}$ from their values at the previous step[1]. Two different algorithms have been implemented and tested during the tp4-project: the leap-frog method and the boris algorithm [1]. It has been proved that the Boris algorithm, which is an implicit scheme, is adequate for this set of equations. The equations of motion discretized with this algorithm are:

$$\left\{ \begin{array}{c} \frac{\vec{r}^{(n+1/2)}-\vec{r}^{(n-1/2)}}{\Delta t} = \vec{v}^{n} \\ \frac{\vec{v}^{(n+1)}-\vec{v}^{n}}{\Delta t} = \vec{E}(\vec{r}^{(n+1/2)}) + \frac{\vec{v}^{(n+1)}+\vec{v}^{n}}{2} \times \vec{B}(\vec{r}^{(n+1/2)}) \end{array} \right. \tag{2.21}$$

Solving the first equation is straight forward. However, the second equation is less trivial, because both $\vec{E}$ and $\vec{B}$ are involved, and the scheme is implicit. The idea here is to separate the effect of the electric field and the effect of the magnetic field [1]. In order to do that, two vectors $\vec{v}^-$ and $\vec{v}^+$ are created:

$$\vec{v}^{n} = \vec{v}^{-} - \frac{\vec{E}\Delta t}{2} \tag{2.22}$$

$$\vec{v}^{(n+1)} = \vec{v}^{+} + \frac{\vec{E}\Delta t}{2} \tag{2.23}$$

Now, the vectors $\vec{v}^-$ and $\vec{v}^+$ are only linked through the effect of the magnetic field. The method to find $\vec{v}^+$ from $\vec{v}^-$ is obtained through geometric considerations on the angles between different vectors. We define Γ as the angle of rotation between the vectors $\vec{v}^-$ and $\vec{v}^+$, and the two vectors $\vec{t}$ and $\vec{s}$, both parallel to $\vec{B}$, as:

$$\vec{t} = -\tan(\frac{\Gamma}{2})\hat{b} = \frac{\vec{B}}{2}\Delta t \tag{2.24}$$

$$\vec{s} = -\sin(\Gamma)\hat{b} = \frac{2}{1+t^2}\vec{t} \tag{2.25}$$

A vector $\vec{v}_p$, perpendicular to $(\vec{v}^+ - \vec{v}^-)$ and $\vec{B}$ is then created and depends on $\vec{v}^-$. Finally, the vector $\vec{v}^+$ is obtained from this new vector $\vec{v}_p$ and the vector $\vec{v}^-$ as follows:

$$\vec{v}_p = \vec{v}^{-} + \vec{v}^{-} \times \vec{t} \tag{2.26}$$

$$\vec{v}^{+} = \vec{v}^{-} + \vec{v}_p \times \vec{s} \tag{2.27}$$

---

[1] this technique is well described in ref. [1]

To summarize, at each step, the program defines $\vec{v}^-$ from $\vec{v}^n$, then finds $\vec{v}^+$ from $\vec{v}^-$, and finally uses equation 2.23 to convert $\vec{v}^+$ into $\vec{v}^{(n+1)}$. The error induced by the boris algorithm is on the first order in Δt.

2.2 Test: Conservation of energy

The section presents the tests of energy conservation that have been preformed in different cases, with different potentials, in order to check the validity of the code. These tests of the conservation of the normalised energy (calculated as expressed in Eq. 2.19) have been effectuated in five parts:

1. In cylindrical coordinates, with an analytical potential that depends on r and z, in order to prove that the Boris algorithm used to solve the equations of motion works and conserves energy.
2. With the same analytical potential, but in the tilted coordinate system (thus the potential depends on r and z'), in order to proove that this change of coordinates is well implemented.
3. Since the values of the simulated potential are only known at certain points in the tilted plane, the method of interpolation that gives the value at any position needs to be tested. This has been done by taking the analytical potential, discretizing it on the grid, and then extrapolating the values of E_r and $E_{z'}$ from the discretized values of the potential.
4. Then the energy conservation has been tested with the simulated potential, in the tilted plane, with an interpolation through the points of the grids, but whithout the implementation of the time dependence.
5. Finally, the last test has been performed with the time dependent potential.

2.2.1 Analytical sinusoidal potential

The numerical solving of the equations of motion induces inevitably some errors. If the method of solving the equations is appropriate, the variations in the energy would only be due to these numerical approximations. Since the Boris algorithm is a first order method, these variations of energy should decrease linearly with Δt. This has been tested with an analytical potential (given in cylindrical coordinates) that depends on r and z:

$$\phi(r,z) = sin(k_r r)sin(k_z z) \tag{2.28}$$

and the results are presented on the left part of figure 2.3. The duration of the simulations was D=700 [n.u.] for any Δt. The right part of figure 2.3 presents the results for simulations where the analytical potential is given in the tilted coordinates ($\phi(r,z')$). Again, D=700 [n.u.] for any Δt. The fact that the two graphs are linear proves that the Boris algorithm, and the coordinate system are adequate for this problem.

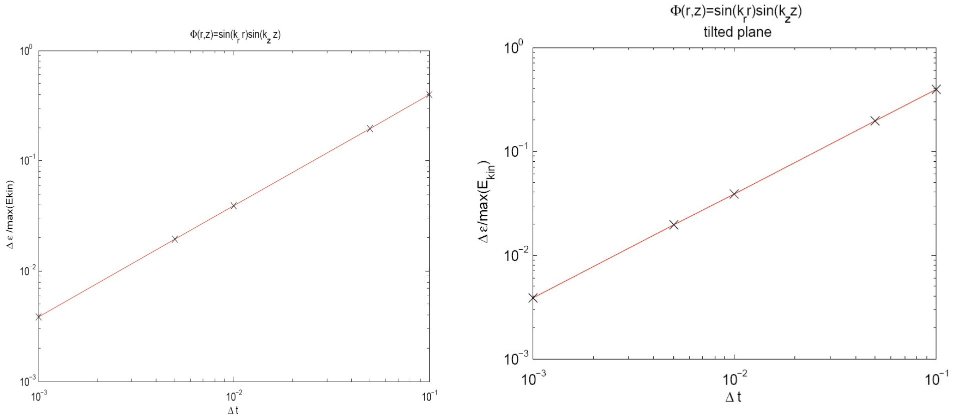

Figure 2.3: variation of energy induced by the Boris algorithm, with a sinusoidal potential. In the first plot, the potential is given in the poloidal plane ($\phi(r,z)$) , and in the second plot, it is given in the tilted plane ($\phi(r,z')$). For any point, D=700[n.u.]

2.2.2 Effect of the discretization

As explained above, the values of the simulated potential are only known on the 256x64 grid points. It has been observed that when we take a sinusoidal potential, discretize it and evaluate it back using an interpolation of the values at the grid points, the simple linear interpolation can only be applied as long as the potential does not change fastly (the variations are such that $K_r\Delta r \simeq 0.02$ and $K_{z'}\Delta z' \simeq 0.1$). However, the simulated potential is varying sometimes very rapidly. Indeed, it has been observed that, in some regions, $K_r\Delta r$ is equal to about 1.5 .

For this reason, a sine function with many oscillations has been considered ($K_r\Delta r$=$K_{z'}\Delta z'$=1.6). With this potential, the variation of energy does not depend on the Δt, but instead it seems to depend on Δr,$\Delta z'$: the grid size in the r- and z'-direction. This is shown in figure 2.4, for Δt=0.01, and $\Delta t = 0.001$. The green lines corresponds to the linear interpolation. They have the same values for both Δt, which means that, in the case of this interpolation, $\Delta\epsilon$ varies with the side of the cells, but does not decrease when Δt decreases.

This effect of the size of the cells cannot be neglected. For this reason, a more accurate method of interpolation, the bicubic interpolation (see Appendix A.1), has been implemented. The two blue lines in figure 2.4 show the values of $\Delta\epsilon$ obtained with this method. One can notice that the values are very close to the error commited by using the analytical solution without any discretization. And, moreover, the variation of energy decreases linearly with the decrease of Δt. For these two reasons, this bicubic method is considered to be adequate, and will be used on the data of the simulated potential.

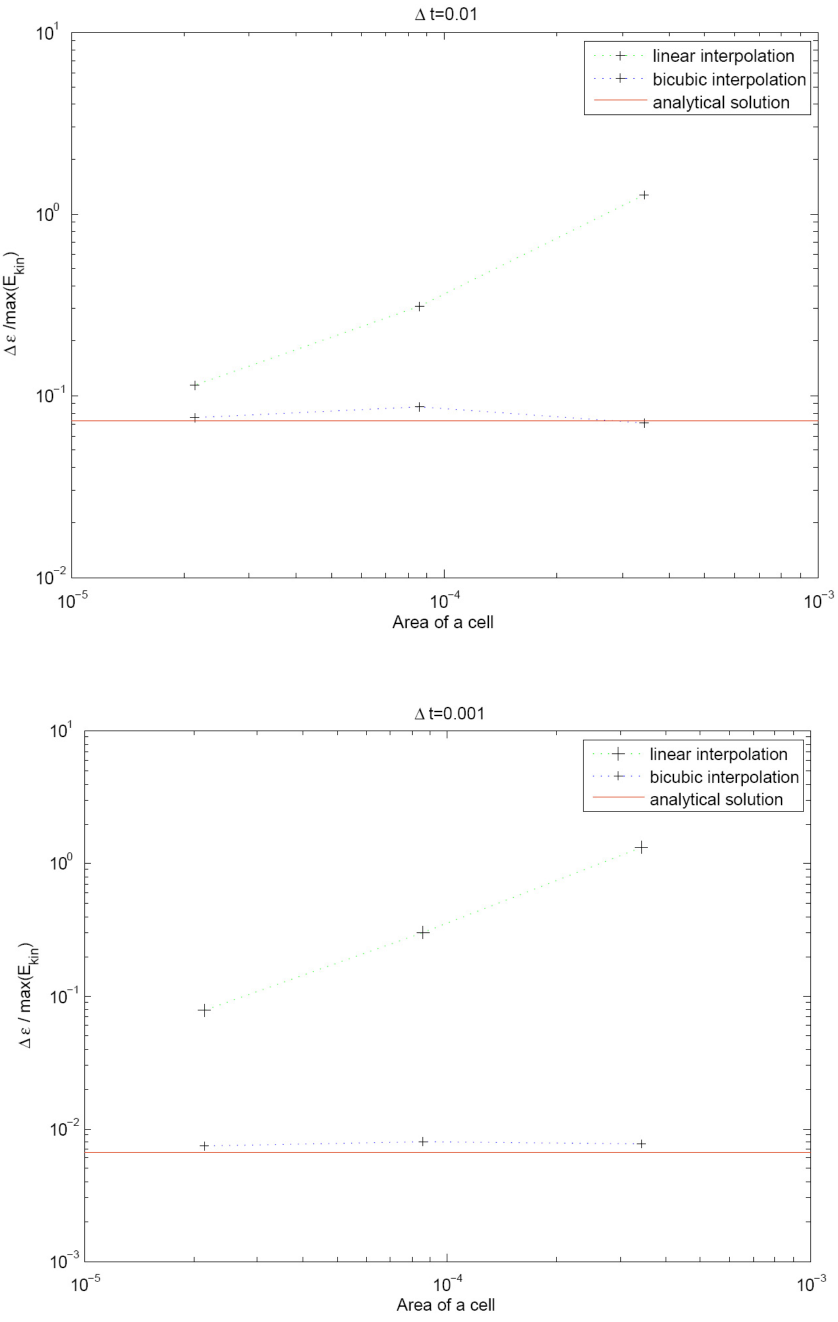

Figure 2.4: Effect of the size of the cells and the method of interpolation on the energy conservation. For any Δt, D=700 [n.u.] .

2.2.3 Conservation of energy with the simulated potential

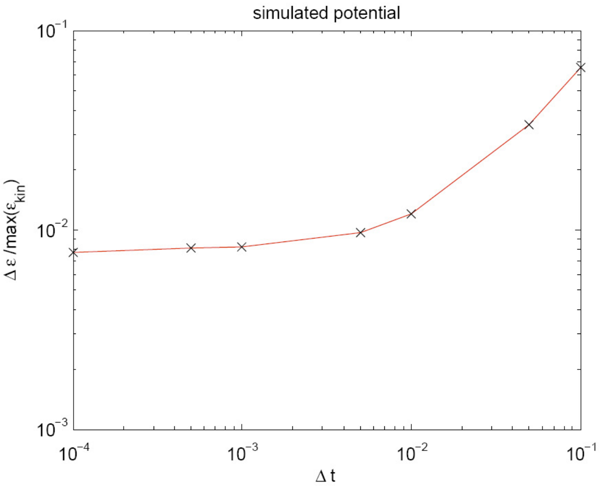

Figure 2.5: Variation of energy for the simulated potential, without the implementation of the time dependence. For any Δt, D=700 [n.u.].

Figure 2.5 presents the variation of energy, with the simulated potential, but without taking into account the time dependence of ϕ. One can see that, for Δt ≥0.01, the variation of energy decreases with the increment of time. However, the curve becomes then a constant. That means that the error induced by Δt becomes negligeable compared to another source of error. This other source is probably the fact that the values of the simulated potential can only be loaded with a precision of 8 digits. Since the potential is saved in a hdf5 file, it is not possible to obtain more precision.

2.2.4 Time dependence of the potential

Finally, the energy conservation has been tested with a potential that depends on t. As explained in section 2.1.2 , this time dependence is numerically calculated by taking linear approximation of the values of $\phi(\vec{x})$, $E_r(\vec{x})$ and $E_{z'}(\vec{x})$ between two successive potential snapshots.

The energy conservation in the case of a time dependent potential can be expressed as:

$$\frac{d\epsilon}{dt}(\vec{x}(t),t) = \frac{\partial\phi}{\partial t}(\vec{x}(t),t) \tag{2.29}$$

The variation of the term $\frac{d\epsilon}{dt}(\vec{x}(t),t) - \frac{\partial\phi}{\partial t}(\vec{x}(t),t)$ is presented in figure 2.6, for different Δt. The plot is very similar to the one with $\phi \neq \phi(t)$. Again, the saturation of the energy conservation accuracy is probably due to a limit in the calculation coming from the number of digits.

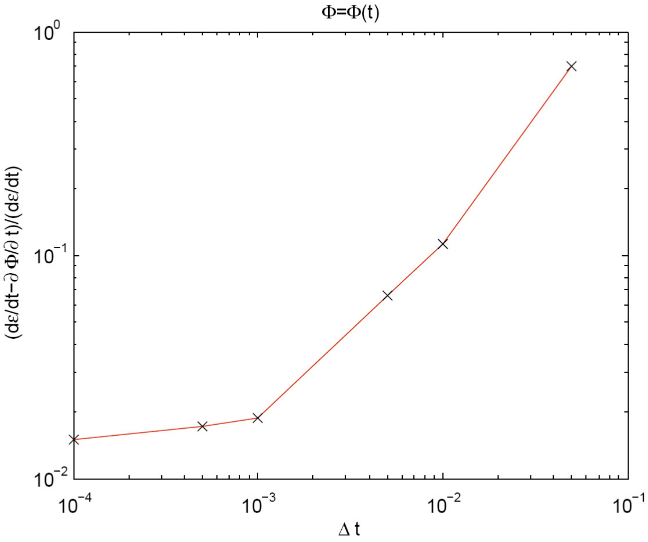

Figure 2.6: Conservation of energy, in the case of a potential depending on t. For any Δt, D=700 [n.u.] .

From figure 2.6, the value of Δt appropriate for this simulation can be chosen. It has to be small enough to provide a good energy conservation, but not too small, since it increases the computational cost of the simulation. By observing figure 2.6, it comes out that it is not useful to consider a Δt<0.001. A comparison of the trajectories with $\Delta t = 0.001$ and $\Delta t = 0.01$, has been performed, and they were similar enough to decide that it was acceptable to run with $\Delta t = 0.01$, even if this gain in the time of simulation induces a small loss of accuracy in the energy conservation. This corresponds, in real units, to a Δt equal to 8.3 ns.

2.3 Implementation of a distribution of particles

2.3.1 The source

The real source in the TORPEX experiment is constructed to generate fast ions with a certain velocity v_0. In reality, the velocities will be distributed in a certain interval around v_0. For this reason, in this simulation, the values of the velocities are chosen following a gaussian curve centered on v_0 and with a standard deviation of typically $\sigma = 5\%$ of v_0. Figure 2.7 presents a typical distribution in velocities for a population of ions, with an energy of T=0.75 .

The two other parameters of the experiment are the initial position of the source x_0, and the vertical inclination of the source α_0 (angle with the horizontal plane). We assume the presence of a spread, both in the horizontal and in the vertical plane. Thus, in the simulation, the angle between the initial velocity of each particle and the horizontal plane (α) will follow a gaussian distribution centered on α_0 and with a standard deviation $\sigma=$ typically 0.1 rad. $\simeq 5.73$ degrees. Finally, the angle in the horizontal plane (β) will also follow a gaussian curve, centered on 0, and with a σ always equal to the one in the vertical plane. The gaussian distributions of initial velocities and initial angles are obtained using the metropolis algorithm, described in Appendix B.

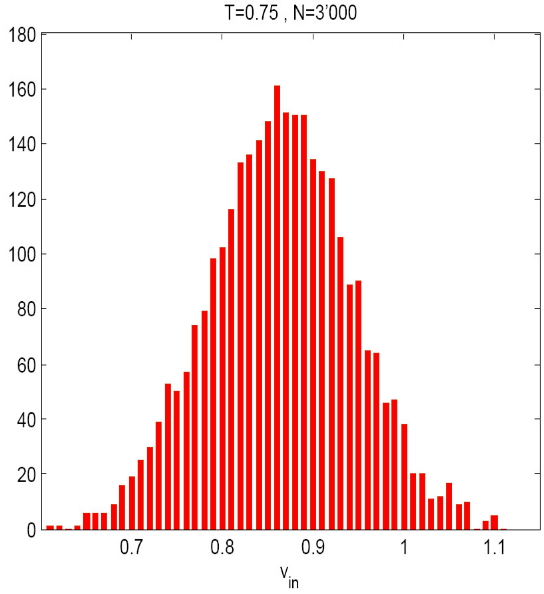

Figure 2.7: Initial velocity distribution of 3'000 particles, for T=0.75=750 eV.

2.3.2 Correlation of $\phi(t)$

We are interested in the statistical evolution of a distribution of particles depending on the turbulence and we want to avoid that the results depend on the specific configuration of the potential at a precise time. Indeed, in the experiment, the exact configuration of the potential is not known, and moreover, the particles do not start exactly at the same time. For this reason, it is more accurate to study an average effect of a potential, than the effect of the potential given at a particular time.

That is why the last improvement of the simulation done for this project is to start a shot of 100 particles in a configuration of the potential, and the another set of 100 in another configuration, and so on, until we obtain a total number of N particles (usually, for reasons of convergence of the distribution explained in chapter 4, N≥3'000). The N particles have small differences in their initial conditions due to the source effect, and small differences in the potential felt along their trajectories.

From the simulations of ref.[15], the evolution of one potential (in the interchange mode), during a long period of time can be known. The idea for the implementation is therefore to load the potential for each set of 100 particles from the same simulated potential, but at different times. The number of unit of time between two shots has

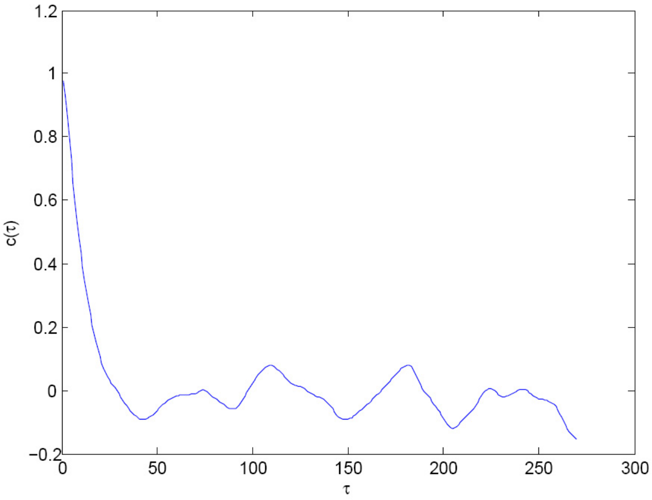

Figure 2.8: Correlation function of the value of the potential at the center of the zone, calculated using 2712 measurements of $\phi(t)$, which corresponds to studying a period of time of 0.0073 s.

to be big enough so that the potential for a generic set i is not correlated with the values of the potential for the previous set (i-1). In order to find the right number of potential snapshots that should be waited between two shots, figure 2.8 presents the evolution of the correlation factor (see Appendix A.2) of $\phi(\vec{x}=0,t)$. One can see that, after about 30 measurements of the potential, the values of $\phi(\vec{x}=0,t)$ are decorrelated. This corresponds, in real unit, to a delay between each shot of 100 particles of:

$$T_{\text{decorr}} = 30 \cdot 2.7[\mu s] = 81[\mu s] \tag{2.30}$$

This value is comparable to the invert of the linear growth rate of instabilities. Indeed (see section 1.2),

$$\begin{aligned} \gamma &= \frac{\sqrt{2}\, c_s}{\sqrt{R\, L_p}} = \sqrt{2} \cdot \sqrt{\frac{T_e}{m_i\, R\, L_p}} && (2.31) \\ &= 6.923 \cdot 10^4 [1/s] && (2.32) \end{aligned}$$

Where the values of T_e and L_p have been evaluated from pressure and temperature profiles obtained for the simulated potential. Thus,

$$\frac{1}{\gamma} = 14.4[\mu s] \tag{2.33}$$

Chapter 3

Results for a single particle

This chapter presents the results obtained for a single particle trajectory. It starts with the observations of the effect of the magnetic field and the electric field on the particle, depending on its initial energy. Then, the values obtained for the velocities along different trajectories are compared with the guiding center equations. The last section presents some chaotic behaviors observed in a single particle motion.

3.1 Study of a trajectory

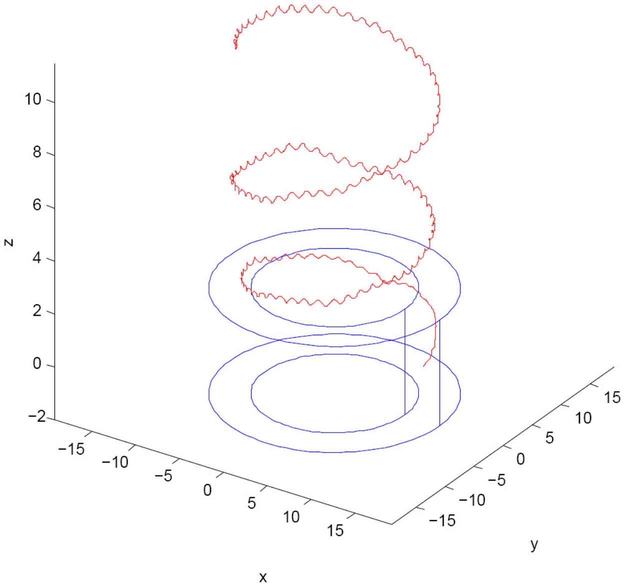

Figure 3.1: 3D view of a fast particle trajectory, for T=0.05=50 eV, D=700, $\Delta t = 0.01$ and ϕ depending on time, and the source is oriented horizontally.

In the data analysis of the two follow chapters, the device TORPEX is considered as extending infinitely in the vertical direction, in order to facilities the study of the statistical properties of the particles motion. A typical trajectory of a single

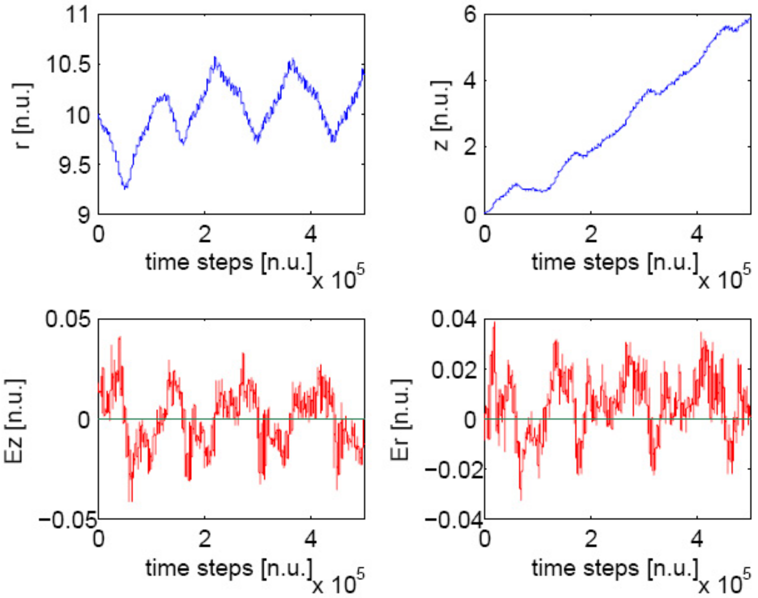

Figure 3.2: Trajectory and electric field, T=0.025=25eV, with ϕ independent of t, and the source is oriented horizontally.

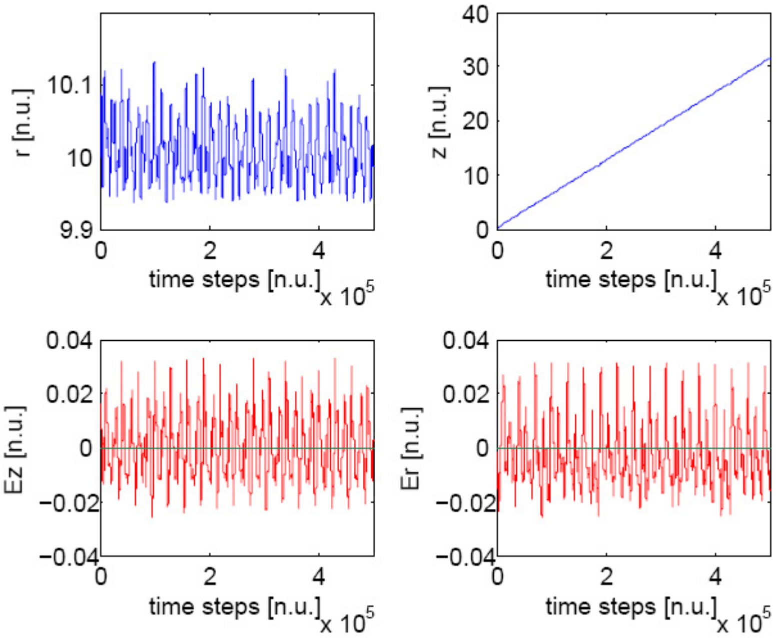

Figure 3.3: Trajectory and electric field, T=0.5=500eV, with ϕ independent of t, and the source is oriented horizontally.

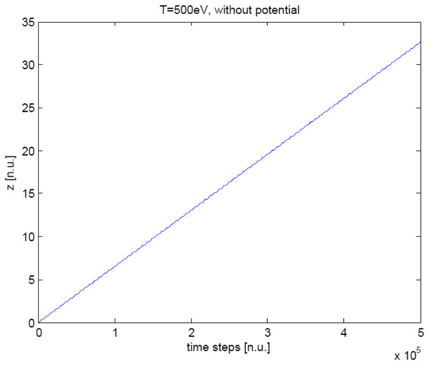

Figure 3.4: vertical component in a motion without potential, T=0.5=500eV, and the source is oriented horizontally.

particle in the presence of a stable magnetic field, and an electric field coming from a potential subject to turbulence driven by interchange instabilities is presented in picture 3.1.

The particle exhibits a fast Larmor motion in the plane r-z' and a slower motion which corresponds to the motion of its guiding center. This second motion depends, as seen in section 1.1, on the $\vec{E}$ field, on the $\vec{\bigtriangledown}\vec{B}$-drift and on the curvature. To observe this two separate motions, figures 3.2 and 3.3 show the variations of the r-component and the z-component of the particle position as a function of time; for particles with different initial energies. These plots are presented in the $(\hat{e_r}, \hat{e_\varphi}, \hat{e_z})$ coordinate system. In order to underline the simple effects, these plots have been obtained for simulations with a potential independent of time.

From figures 3.2 and 3.3, we see that the radial motion is affected by two separate effects. First, the slow oscillations with large amplitude are directly linked to the sign of the $E_{z'}$ field felt by the particle at this moment. Indeed, the fact that $E_{z'}$ changes sign depending on the position of the particle causes the $\vec{E} \times \vec{B}$-drift to act in the opposit direction; and this explains the changes of direction in the r-motion. The second noticeable effect is the small fast oscillation of r(t). This is a manifestation of the Larmor motion. About the z-component, we have again the small oscillations due to the Larmor motion, the $\vec{E} \times \vec{B}$-drift, and an effect of the $\nabla\vec{B}$ and the curvature that makes the particle go up (in addition, of course, to the fact that the particle follows the magnetic field lines).

It is noticeable that, when the velocity of the particle increases, the $\vec{E}$ field felt by it changes sign more rapidly because the particle travels more rapidly from regions where $\vec{E}$ is positive to regions where $\vec{E}$ is negative. Thus, the oscillations in r and z are faster, and the amplitude of these oscillations is smaller. Therefore, the effect of the electric field on the particle trajectory decreases as the energy of the particle increases. Figure 3.4 presents the evolution of the vertical component of the trajectory, with an energy of T=0.5, but without introducing a potential. We

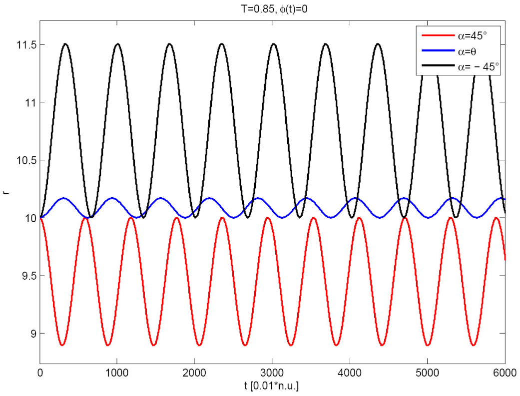

Figure 3.5: Evolution of the radial component of different trajectories, depending on the angle α between the initial velocity and the horizontal plane. θ represents the inclination of the magnetic field lines

can see that this plot is very similar to the right-up of figure 3.3. This means that, at this energy, the effect of the electric field is negligible compared to the effect of the magnetic field. However, this is not true when the potential varies in time. In this case, the effect of the electric field still decreases as the energy of the particle increases, but is never totally negligible.

3.1.1 About the Larmor rotation

A characteristic of the Larmor rotation is the fact that if the angle between the initial velocity and the magnetic field lines (whose inclination is θ) is positive, the particle will starts to rotate in the direction toward the center of the torus (high field side), whereas if the angle is negative, the particle will rotate toward the outside of the torus (low field side). This effect is presented in figure 3.5 for three particles starting at the same position, with the same initial velocities corresponding to T=0.85, in the simple situation where the particles experience only the effect of the magnetic field (no potential). Furthermore, since the particle rotates in a different region of the torus depending on its initial direction, then it will experience a different value of $\vec{B}$. Since the Larmor radius is inversely proportional to $\vec{B}$, the Larmor radius of a particle will be bigger if the particle rotates in a low field side region (so if its initial angle α is smaller than θ), than if it rotates in a high field side region (α bigger than θ). This difference in the Larmor radius is also clearly observed in figure 3.5.

In figures 3.2 and 3.3, the Larmor motion of the particle was expected to be much bigger for high initial energy (since $\lambda_L \propto v_0$). This is not observed because, in these particular cases, the initial velocity is almost parallel to the magnetic field lines, and only the component of the velocity perpendicular to $\vec{B}$ plays a role in the Larmor motion.

An interesting particular case is the situation where the particle starts with a velocity exactly parallel to the magnetic field lines. It has been observed that, when there is no electromagnetic potential, the particle that starts with the velocity paralel to the magnetic field lines experiences almost no Larmor oscillation. Its velocity stays mainly parallel to the field lines. However, as soon as the particle feels a small electric field, in the r- or z'-direction, this induces a small displacement in the r-z' plane, that leads to the creation of a perpendicular velocity, with induces a non-negligible Larmor rotation proportional to the initial energy of the particle.

3.1.2 Comparison with the guiding center equations

In this simulation, the three equations that give the velocity of the guiding center of a particle, from the parallel and perpendicular velocities of this particle (in the tilted coordinates system), can be easily calculated from the theory presented in section 1.1 . It gives:

$$v_r(t) = -\frac{r}{R} E_{z'}(\vec{x}, t) \tag{3.1}$$

$$v_{z'}(t) = \frac{r}{R} E_r(\vec{x}, t) + \frac{1}{r}(\frac{v_\perp(t)^2}{2} + v_\parallel(t)^2) \tag{3.2}$$

$$v_{\varphi'}(t) = v_{\parallel \text{in}} \tag{3.3}$$

where the electric field field is evaluated at the particle position at a given time t and $v_\perp$(t) and $v_\parallel$(t) are the decomposition of the particle velocity at time t. The main assumption for the validity of the guiding center model, presented in section 1.1, is that the potential does not vary much on the area a Larmor rotation, which is satisfied when the amplitude of the potential is small and when the Larmor radius of the particle (depending on its initial energy and the inclination of the source) is small.

According to the GC theory, $v_{\varphi'}$, which is the velocity of the guiding center parallel to the field lines, is conserved. Figure 3.6 presents the comparaison of the velocity of a particle with the velocity given by the equations of its guiding center, in two cases: one with T=0.08=80 eV, and one with T=1 keV. In both cases, the particle starts with a velocity exactly parallel to the magnetic field lines. We can observe that the conservation of $v_\parallel$ is better in the case at small temperature. This says that the GC assumption is less valid when T is high, which was expected since λ_L increases when T increases. However, in both plots, the velocities in the r- and z'-directions are comparable. This tells us that, for the range of energy that we are considering (100-1000 eV), the trajectory of one particle can be approximated by the trajectory predicted by the equations of its guiding center. This fact will be used in the approximation of the motion of the center of mass of a statistically meaningful distribution of particles. When the source is not parallel to the magnetic field lines, this replacement can still be effectuated, as long as the energy of the particle is not too high. Indeed, λ_L has to be kept inferior to a certain value (expressed in section 1.1), and an increase in the inclination of the source, will increase the initial perpendicular velocity and therefore increase λ_L.

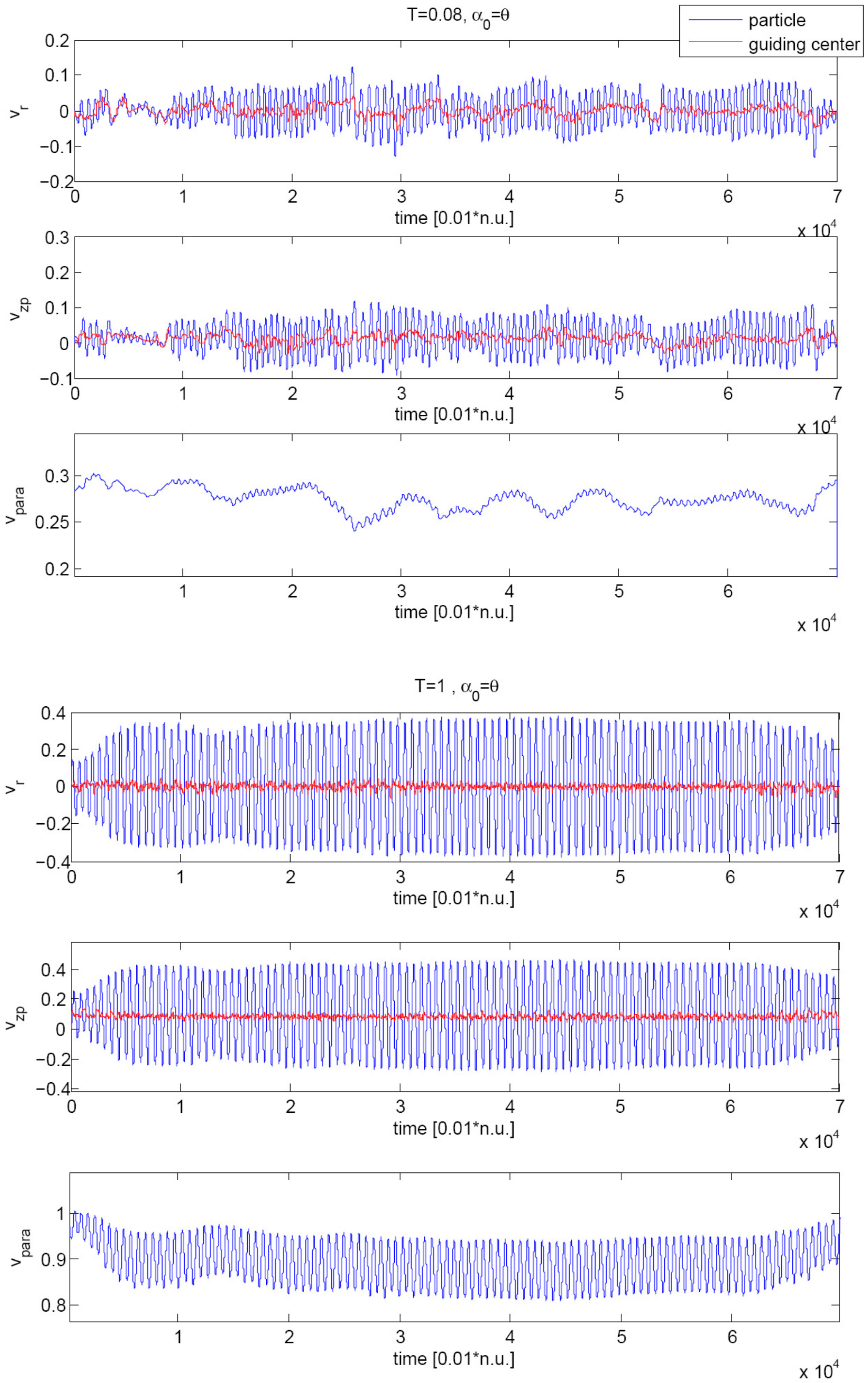

Figure 3.6: Comparisons of the velocities for a single particle, at T=0.08=80 eV and T=1=1000eV.

The conservation of energy gives a second method to check if the GC assumption is respected. We have seen in the previous chapter that the equation of energy conservation

$$\frac{d}{dt}(\frac{1}{2}v^2 + \phi) = \frac{\partial \phi}{\partial t} \tag{3.4}$$

is respected in this simulation. Now, we can make the simplification $v_{\|}$=constant and test if the energy is still conserved. If it is, this means that $v_{\|}$ is indeed a constant, which tells us that the GC assumption is respected. With this simplification, the expression of the energy conservation becomes:

$$\begin{aligned} \frac{d}{dt}(\frac{1}{2}v_{\perp}^2) &= \frac{\partial \phi}{\partial t} - \frac{d\phi}{dt}(x(t), y(t), z(t), t) && (3.5) \\ &= \frac{\partial \phi}{\partial t} - \frac{\partial \phi}{\partial t} - \vec{v}\vec{\nabla}\phi && (3.6) \\ &= -v_r E_r - v_{z'} E_{z'} && (3.7) \end{aligned}$$

It has been checked that, along the trajectory of one particle, the values of the quantity

$$A = \frac{1}{2}(\frac{v_{\perp}^2(t) - v_{\perp}^2(t-1)}{\Delta t}) + v_r(t)E_r(t) + v_{z'}(t)E_{z'}(t) \tag{3.8}$$

is limited into a certain range. The size of the interval in which the quantity A oscillates decreases linearly with the initial energy of the particle, and decreases also linearly with the intensity of the potential. This proves that the assumption $v_{\|}$=constant is more accurate when the potential is small or when the initial energy of the particle is small. We recognize the hypothesis of validity of the GC model.

3.2 Chaotic motion

It has been observed that the motion of a fast particle in the simulated plasma is chaotic. This section presents two characterizations of this phenomenon. A more detailed study of this chaotic behavior would go beyond the goal of the present project.

3.2.1 Sensitivity to the initial conditions

The first thing that caracterizes a chaotic behavior is the high sensitivity to the initial conditions [8]. It has been observed that the oscillations in r presented in the previous section are very sensitive to the initial conditions. They are particularly sensitive to the initial velocity, the initial position, and the Δt used in the integration. This is shown in figure 3.7,

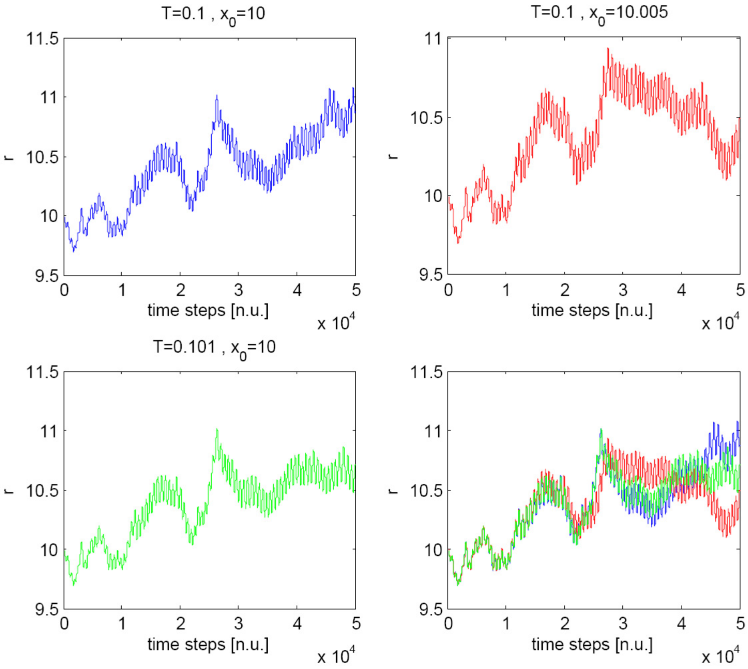

Figure 3.7: Evolution of the r-coordinates of trajectories with different initial conditions, with $\phi = \phi(t)$.

3.2.2 Loss of memory

Another diagnosis of chaos is the loss of memory along a signal [8]. This phenomenon can be revealed by the study of the correlation factor along the signal (see Appendix A.2). When there is loss of memory, the signal does not remember its antecedent values, so the correlation factor decreases. The fact that $c(\tau)$ tends to 0 when τ tends to ∞ is a proof that the signal is chaotic. To be more precise, $c(\tau)$ follows [8]:

$$c(\tau) \propto e^{-\gamma\tau} \tag{3.9}$$

where γ is a good indicator of the degree of loss of memory in the signal. The bigger γ is, the more chaotic the signal is. This has been applied on the r-coordinate of a trajectory, for simulations with two different energies. The results are presented in figure 3.8, where the solid curves represent the evolution of the correlation factors, and the curves in dots are the exponential approximations. It comes out that γ is bigger when the energy is small. This was expected, because, when T is small, the effect of the $\vec{E} \times \vec{B}$-drift is more important. The oscillations that appear on the two solid curves are due to the Larmor rotation.

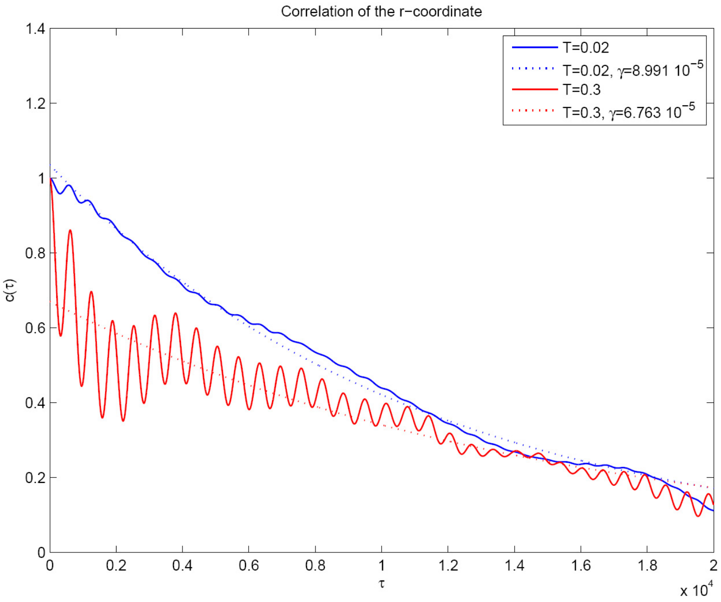

Figure 3.8: Correlation factor of the r-coordinate of two trajectories, one with T=0.02=20 eV, and the other with T=0.3=300 eV, which $\phi = \phi(t)$

Chapter 4

Results for a distribution of ions

The previous chapter presented the study of the motion of a single particle, in our particular geometry, with realistic fields and potential. The next step of the project is to obtain the data for a statistical set of particles, and study their global behavior. The first section of this chapter is dedicated to the choice of the number of ions considered. Then, the description of the evolution of a gaussian distribution in 3-dimensions is divided in two parts: the study of the evolution of the center of mass (presented in the second section of this chapter), and the study of the spreading of the distribution in the 3 directions $\vec{e_i}$ (i=r,z',φ'), which is the subject of the last section of the chapter.

4.1 Number of ions

The number of ions implemented is a parameter that needs to be chosen carefully. Indeed, statistical convergence should be reached, but the number is limited by the computational cost. In the data analyis, a main interest will be put on the spreading of the ions in both parallel, and perpendicular directions. Therefore, an important physical quantity will be the standard deviation $\sigma_i(t,N)$ in the direction $\vec{e_i}$ (i=r,z',φ') defined as:

$$\sigma_i^2(t,N) = \frac{1}{N}\sum_{j=1}^{N}[\delta r_{j_i}(t)]^2 \tag{4.1}$$

where $\delta r_{j_i}(t) = r_{j_i}(t) - r_{cm_i}(t)$ is the distance from the i-coordinate of the particle j to the i-coordinate of the center of mass, at time t.

Figure 4.1 presents the evolution of the standard deviation in the three directions, for different energies, as a function of the number of particles. The detection has been done at a precise time Tdetect=110 n.u. The spreads in the r, z' and φ' directions converge after considering about 1000 particles, however it has been chosen to run the usual simulations with N=3'000. For small energies (under 0.05=50 eV), more than 3'000 particles are necessary in order to obtain convergence. For this reason, those simulations use N=10'000, and sometimes even more.

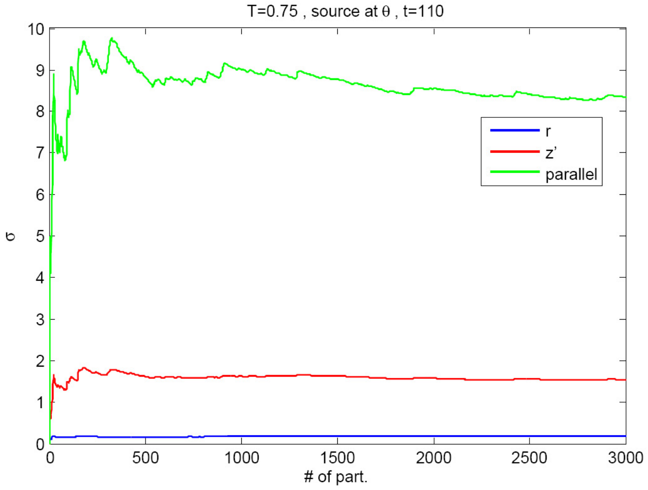

Figure 4.1: Standard deviation as a function of the number of particles, for T=0.75=750 eV.

4.2 Study of the motion of the center of mass

An important quantity that characterizes the evolution of a distribution of particles is the position of its center of mass, $\vec{x}_{cm}$. The position of a particle i is expressed, in the tilted coordinates system as:

$$\vec{x_i} = r_i \hat{e_r} + r_i \varphi_i' \hat{e_{\varphi'}} + z_i' \hat{e_{z'}} \tag{4.2}$$

It follows that the center of mass of a distribution of N particles is defined in the $\{e_r, e_{z'}, e_{\varphi'}\}$ coordinates system as:

$$\vec{x}_{cm} = \frac{1}{N} \sum_{i=1}^{N} \begin{pmatrix} r_i \\ r_i \varphi_i' \\ z_i' \end{pmatrix} \tag{4.3}$$

4.2.1 motion along r and z'

Figure 4.2 presents the evolution of the r- and z'- components of the center of mass, for different cases. For these plots and for the further data analysis, the time between two measurements of the positions and velocities of the particles is chosen to by equal to dT_{detect} =2 times the normalized unit of time, which corresponds to a measurement every 200 steps.

Figure 4.2 shows that the center of mass oscillates in the r- and in the z'-direction. (The oscillation when the source is parallel is, in certain cases, too small to be noticed on the plots.) The amplitude of the oscillations depends on the inclination of the source (i.e. on the component of the initial velocity that is perpendicular to the field lines) and on the energy of the particles; and it decreases with time. It has been checked that the period of the oscillations is exactly equal to the Larmor

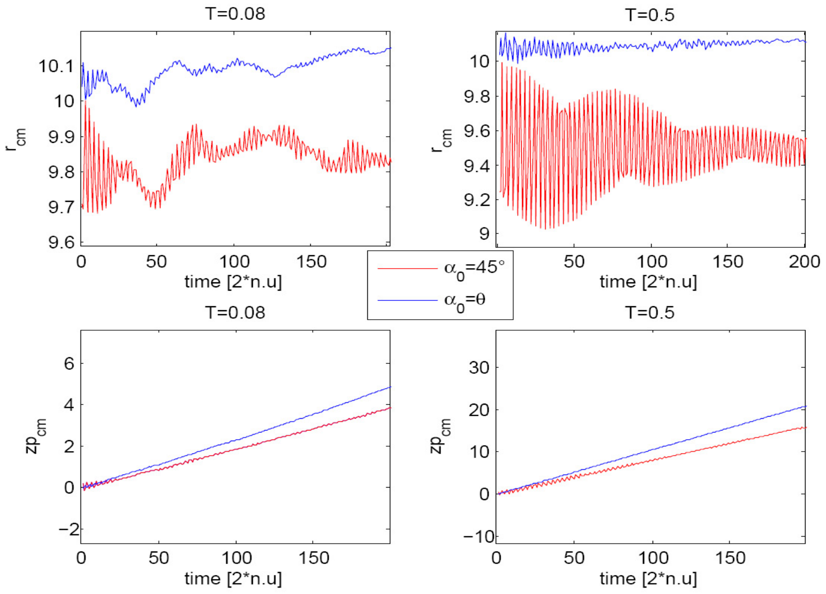

Figure 4.2: An example of the evolution of the r- and z'- components of the center of mass, for different energies and different inclinations of the source.

rotation period, and the amplitude of the oscillation is smaller than the theoretical Larmor radius of each particle, because the particles are not necessarily in phase. The amplitude of the oscillations decreases with time, because the cloud of particles looses coherence. The fact that the radial position of the center of mass is smaller when the source is tilted (with a positive angle) is a consequence of the fact that, in this case, each particle starts to rotate toward the low field side (section 3.1.1) .

The vertical motion of the center of mass is mainly due to the $v_{\vec{\nabla B}}$-drift and the curvature drift, but there is also an effect of the $v_{\vec{E}_r\times\vec{B}}$-drift, since in these simulations, $<v_{\vec{E}_r\times\vec{B}}>\neq 0$. The vertical velocity of the center of mass becomes smaller when the inclination of the source increases. This is due to the fact that the vertical motion of each particle depends on $v_\parallel^2$, but only on $v_\perp^2/2$, and an inclination of the source will increase $v_\perp$ of each particle and decrease its $v_\parallel$. The $v_{\vec{E}_r\times\vec{B}}$ effect does not depend on the inclination of the source, but on the region of the poloidal cross section covered by the cloud of particles.

4.2.2 Comparison with the guiding center equations

The velocity of the center of mass is:

$$\vec{v}_{cm} = \frac{d}{dt}\vec{x}_{cm} = \frac{d}{dt}\frac{1}{N}\sum_{p=1}^{N}\vec{x}_p = \frac{1}{N}\sum_{p=1}^{N}\underbrace{\frac{d}{dt}\vec{x}_p}_{=\vec{v}_p} \tag{4.4}$$

As seen in section 3.1.2, when the GC assumption is valid, one can replace the velocity of each particle by the velocity of its guiding center. The approximate velocity of the center of mass becomes then:

$$v_{r\,cm,gc}(t) = \frac{1}{N}\sum_{p=1}^{N}(-\frac{r}{R}E_{z'}(\vec{x}_p,t)) \tag{4.5}$$

$$v_{z'\,cm,gc}(t) = \frac{1}{N}\sum_{p=1}^{N}(\frac{r}{R}E_r(\vec{x}_p,t)+\frac{1}{r}(\frac{v_\perp(t)^2}{2}+v_\parallel(t)^2)) \tag{4.6}$$

$$v_{\varphi'\,cm,gc}(t) = v_{\parallel \mathrm{in}} \tag{4.7}$$

Figure 4.3 presents the comparison between the velocity of the center of mass, and the velocities calculated using equations 4.5 and 4.6, at two different energies, with the source parallel to the magnetic field lines. We see that the velocities of the center of mass follow an oscillation due to the Larmor motion (same period). This oscillation tends to disappear with time because the cloud looses coherence. The guiding center does not follow this oscillation (which is consistant with the definition of the guiding center). Except for that, $\vec{v_{cm}}$ and $\vec{v_{cm,gc}}$ in the plane perpendicular to the field lines are very similar. On the plots of $v_{z'}$ at high energy, a shift appears between the velocity of the center of mass and the velocity given by the above equations. This shift comes only from the evaluation of $v_\perp$ and $v_\parallel$ of each particle. Indeed, in this data analysis, measurements have only been taken every dT_{detect} =2. Therefore, an important mistake is generated when the velocities are simply evaluated by finite differentiation of the particles positions. This problem did not occur in the analysis on a single particle trajectory, because there measurements were taken every 0.01 n.u. , so the approximation of $v_\perp$ and $v_\parallel$ were more accurate.

It is noticeable that the parallel velocity of the center of mass is better conserved than the parallel velocity of a single particle. This can be explained by the fact that the high number of particles considered has an effect of averaging the variations of ϕ. The conclusion of this comparison is that the approximation of the trajectory of the center of mass with the expressions using the guiding center equations of each particles (4.5 and 4.6) is valid on all the interval of energies considered, when the source is parallel to $\vec{B}$.

4.2.3 Approximation of the evolution of the center of mass

An interesting problem is to find an approximation of the motion of the center of mass that depends only on the initial velocities of the particles and on the simulated potential. This approximation could give a prediction for the location of the detector in the real experience on TORPEX. The approximation has only been calculated for the case when the source is parallel to the magnetic field lines.

It has been shown in the last subsection that the velocities of the center of mass can be replaced, at all energies, by the expressions using the guiding center velocities of each particles (4.5 and 4.6). It follows that the parallel velocity of the center of mass is about constant, and, in order to estimate the perpendicular velocity, one only has to find an approximation of the equations 4.5 and 4.6. The first step for

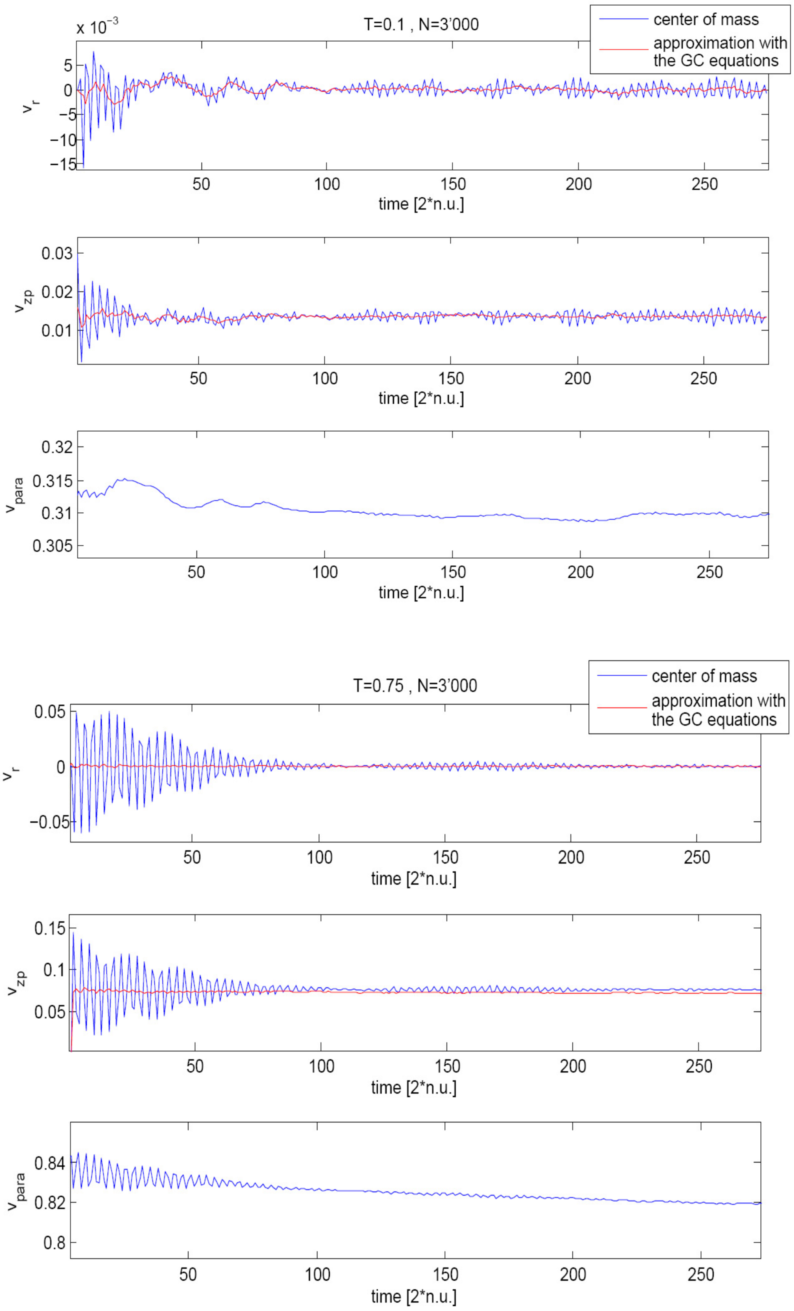

Figure 4.3: Comparison of the velocities of the center of mass (blue curves) with the ones of the guiding center (red curves), for 3'000 particles, with an initial energy T=0.1=100eV and T=0.75=750eV

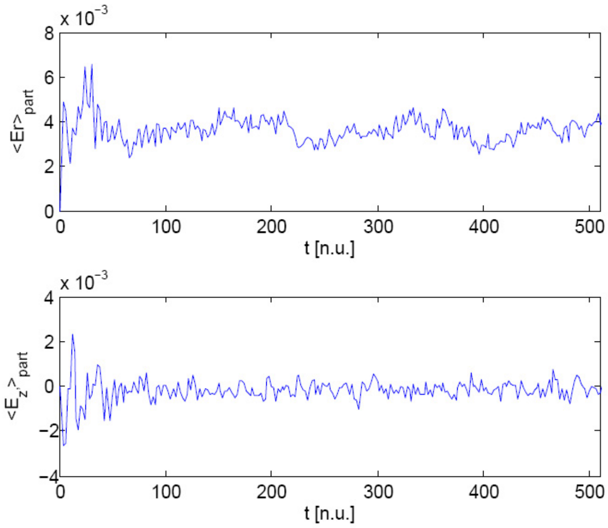

Figure 4.4: Average of the electric field felt by each particle of a distribution with initial energy T=0.5 vs time.

that is to replace the radial position of each particle at a given time r(t), by R, the center of the poloidal section. Equations 4.5 and 4.6 become then:

$$v_{r\,cm,gc} \sim \; < E_{z'}(t) >_{part.} \tag{4.8}$$

$$v_{z'\,cm,gc} \sim \; < E_r(t) >_{part.} + \underbrace{\frac{1}{N}\sum_{p=1}^{N}\frac{1}{R}\left(\frac{v_{\perp_p}^2(t)}{2} + v_{\parallel_p}^2(t)\right)}_{K} \tag{4.9}$$

The next step is to give an estimation of the values $< E_r(t) >_{part.}$ and $< E_{z'}(t) >_{part.}$, the mean electric fields felt by the particles at a given time. It would be pleasant to neglect the time dependence of those averages. In order to determine if this is acceptable, figure 4.4 presents the evolution in time of the electric fields averaged on a distribution of 3'000 particles, with T=0.5 . We see that, after a relatively short time, the mean electric fields become constant. The time to reach the equilibrium depends on the energy of the particles, but represents, in any case, less than one turn in TORPEX. The value of the equilibrium ($< E_r(t) >_{part.}$ and $< E_{z'}(t) >_{part.}$) can be found by simply averaging in time. It comes out, for the simulation at T=0.5, that $< E_r >_{part.}$=0.0036 [n.u.] and $< E_{z'} >_{part.}$=-0.00016[n.u.].

Since the final objective is to obtain an approximation for the motion of the center of mass that depends only on the considered potential, it would be necessary to replace the expressions $< E_r >_{part.}$ and $< E_{z'} >_{part.}$ by average fields that don't depend on the particle positions. This average field can be calculated for E_r from the radial profile of the turbulent potential averaged in time, and in the vertical direction. This profil is presented in the upper part of figure 4.5. The lower part of the picture presents the derivative with respect to r of this averaged potential (with

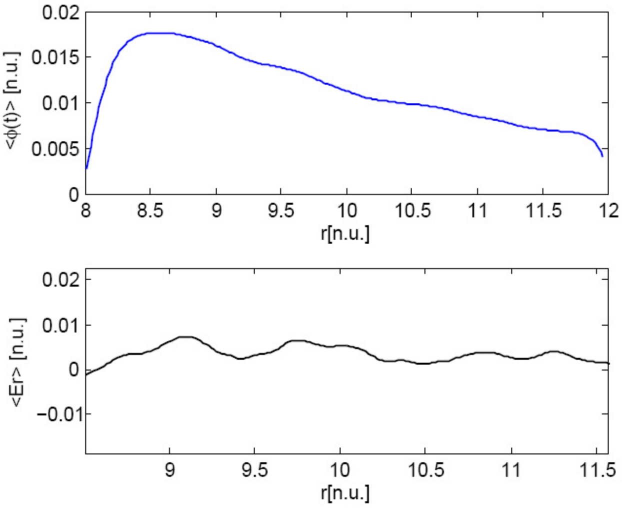

Figure 4.5: Mean values of $\phi(\vec{x}, t)$ and $Er(\vec{x}, t)$ obtained from the grids of potential by averaging on the z'-direction, and then on 211 time measurements of $\phi(\vec{x}, t)$ (which corresponds to the duration of a typical particle trajectory)

the addition of a minus sign). The average in r of this second profile gives a mean value of $< E_r >= 0.0038$ [n.u.]. The fact that this value is so close to the mean field felt by the particle in the simulation tells us that the averaged field of equations 4.6 and 4.7 can be replaced by a time and z- averaged profile of $-\frac{\partial\phi}{\partial r}$ which does not depend on time, neither on the positions of the particles.

Similarly, $< E_{z'} >_{part.}$ can be replaced by $< E_{z'} >$ that is equal to 0. Indeed, the quantity $< E_{z'} >$ corresponds to the vertical integral of $E_{z'}$ along a zone of potential, so along the distance between two returns of a magnetic field line. Since the interchange instability does not propagate in the parallel direction, the potential is invariant under a rotation of 2π. Therefore, the potential is periodic in the z'-direction. Its period is the return of a magnetic field line, which is equal, by definition, to the height of the zone of potential. We define the points A and B as the lower and upper values of z at a position r given; then,

$$\int_A^B E_z dz = -\int_A^B \frac{\partial\phi}{\partial z} dz = \phi^B - \phi^A = 0 \tag{4.10}$$

It follows that, in this approximation, the center of mass does not move radially. Moreover, in order to have an approximation of the vertical motion, the last task is to find an expression for the term K of equation 4.9 . The approximation of the term containing $< v_{\|_p}^2(t) >_{part.}$ is obvious, since $v_{\|}$ of each particle is constant, and the initial velocity of the particles is only parallel:

$$\frac{1}{R} < v_{\|_p}^2(t) >_{part.} = \frac{1}{R} < v_{\|_p}^2 >_{part.} \sim \frac{T}{R} \tag{4.11}$$

The approximation of the term containing $< v_\perp^2(t) >_{part.}$ is less trivial since the perpendicular velocity comes from a complicated exchange between the kinetic energy of the particles and the energy of the potential. Actually, we will see that, since the source is parallel to the magnetic field lines, $v_\perp << v_\parallel$, and the term $\frac{1}{2R} < v_{\perp_p}^2(t) >_{part.}$ can be neglected. But, in order to prove that this term can be neglected, let's calculate an estimation of it using the expressions of the guiding center velocities and the results that have already been found:

$$\begin{aligned}
< v_{\perp_p}^2(t) >_{part.} &= < v_r^2(t) + v_{z'}^2(t) >_{part.} && (4.12)\\
&= < v_r^2(t) >_{part.} + < v_{z'}^2(t) >_{part.} && (4.13)\\
&\sim < {v_r}_{cm,gc}^2(t) >_{part.} + < {v_{z'}}_{cm,gc}^2(t) >_{part.} && (4.14)\\
&\sim < E_z^2 > + < (E_r + \frac{1}{R}(v_\parallel^2 + \frac{v_\perp^2}{2}))^2 >_{part.} && (4.15)\\
&\sim < E_r^2 > + < \frac{1}{R^2}(v_\parallel^2 + \frac{v_\perp^2}{2})^2 >_{part.} + < \frac{2E_r}{R}(v_\parallel^2 + \frac{v_\perp^2}{2}) >_{part.}
\end{aligned}$$

After neglecting some terms and rearranging, in comes out that:

$$< v_{\perp_p}^2(t) >_{part.} \sim < E_r^2 > + < \frac{1}{R^2} v_\parallel^4 > + < \frac{2E_r}{R} v_\parallel^2 > \quad (4.16)$$

And, by gathering the different estimations, the approximation for the perpendicular velocity of the center of mass is:

$$\begin{aligned}
v_{r\,cm} &\sim < E_{z'} > = 0 && (4.17)\\
v_{z'\,cm} &\sim < E_r > + \frac{T}{R} + \frac{1}{2R}(< E_r^2 > + < \frac{1}{R^2} v_\parallel^4 > + < \frac{2E_r}{R} v_\parallel^2 >) && (4.18)
\end{aligned}$$

Finally, it has been observed from the data of a simulation that, as expected, the third term in the approximation of $v_{z'\,cm}$ is negligible compared to the two first terms. Therefore, the final approximation for the velocity of the center of mass is:

$$\begin{aligned}
v_{r\,cm} &\sim 0 && (4.19)\\
v_{z'\,cm} &\sim < E_r > + \frac{T}{R} && (4.20)\\
v_{\varphi'\,cm} &\sim const. && (4.21)
\end{aligned}$$

The accuracy of this approximation is presented in figure 4.6 for T=0.1 and T=0.75. The approximation was expected to be less good for high energy, because of the guiding center assumptions. However, figure 4.6 shows clearly that the approximation is valid for all the range of energies considered. This is probably due to the fact that some errors coming from the different approximations cancel themselves. If the source was tilted, $v_\perp$ would not be negligible compared to $v_\parallel$ anymore, so the above approximation would not be adequate. This approximation depends only on the potential, and the initial velocity of the particles, as required. However, it is only useful for the prediction of the experiment, if one find a way of approximating the term $< E_r >$, which is a complicated characteristic of the simulated potential.

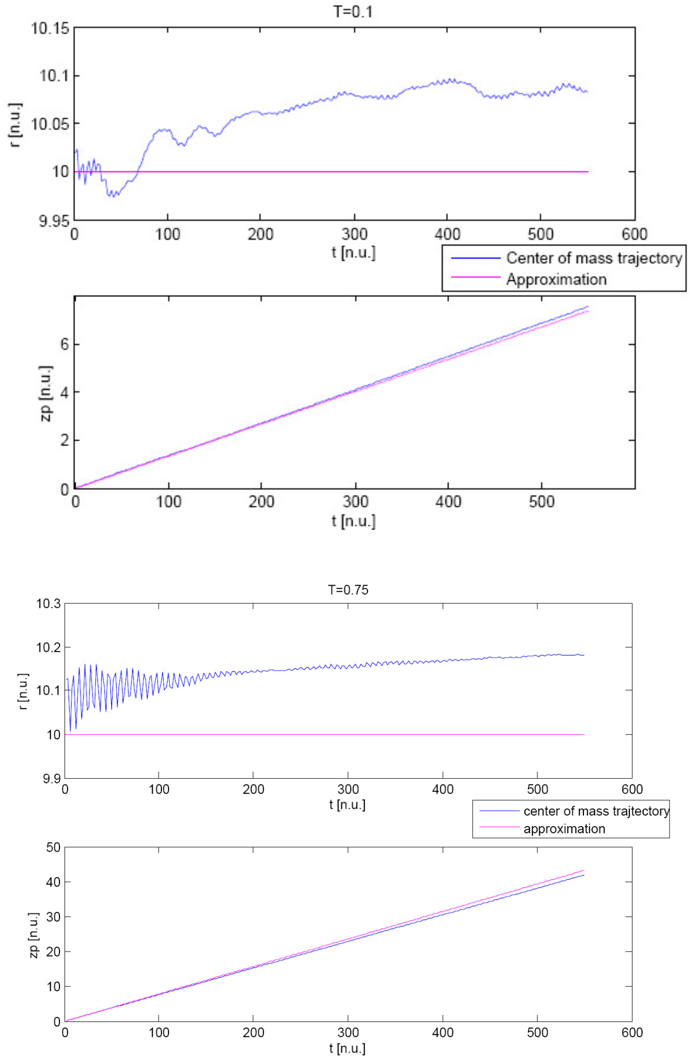

Figure 4.6: approximation of the motion of the center of mass of a distribution of 3’000 particles, for two different energies.

The fact that this approximation of the motion of the center of mass works so well tells us that, in the $\vec{E}\times\vec{B}$-effect, only the mean values of the electric field affects the center of mass. Therefore, the effects of turbulence cannot be detected on the motion of the center of mass.

4.3 Study of the spreading

4.3.1 Method

In order to study the spreading of a gaussian distribution in 3D, we define $\delta r_{j_i}(t) = r_{j_i}(t) - r_{cm_i}(t)$ as the distance from the i-coordinate of the particle j to the i-coordinate of the center of mass, at time t. The evolution of a typical distribution of particles can be studied by plotting the distribution of the $\delta r_{j_i}(t)$ in the three directions, at different times. This has been done for a simulation at T=0.5 and is represented on the left part of figure 4.7. One can notice from this figure a spreading of all the distributions with time. In order to characterize this spreading, it is necessary to study the time evolution of the standard deviation of the distributions, defined as (for a distribution of N particles):

$$\sigma_i^2(t,N) = \frac{1}{N}\sum_{j=1}^{N}[r_{j_i}(t) - r_{cm_i}(t)]^2 \tag{4.22}$$

It has been seen in section 4.1 that, above a center number of particles N, the σ_i^2's converge. For the study presented in this section, the values of σ_i^2 have always been obtained with a number of particles big enough to have convergence. As seen in section 1.3, the standard deviation is assumed to follow the time dependence:

$$\sigma^2(t) \sim t^{\gamma} \tag{4.23}$$

If $\gamma = 1$ the transport corresponds to usual diffusion. If $\gamma < 1$ the transport is sub-diffusive, if $\gamma > 1$ the transport is super-diffusive. The particular case $\gamma = 2$ denotes ballistic spreading, and $\gamma = 0$ corresponds to a case where the distribution of particles does not change in time.

The method used to characterize the transport in each direction from the data of the simulations is to calculate the variation of σ_i^2 with time and to plot it in a log-log scale where the exponent γ can simply be read as the slope of the line. A typical example of these log-log plots is presented in figure 4.8 for a simulation with T=0.5. One can see that, at least in the radial direction, the values corresponding to the beginning of the simulation should not be taken into account because the fluctuations are too important. In this case, the plot of $\log(\sigma_r^2)$ becomes linear after t=140 n.u. which corresponds to the time necessary so that the particles do more than one turn in TORPEX. Moreover, the slope can sometimes be difficult to evaluate. Therefore, the exponents presented in the tables below have to be considered within a certain margin of error.

A possible way of checking the accuracy of the exponents γ's and associate to them a right margin of error is to study the evolution of the probability distribution

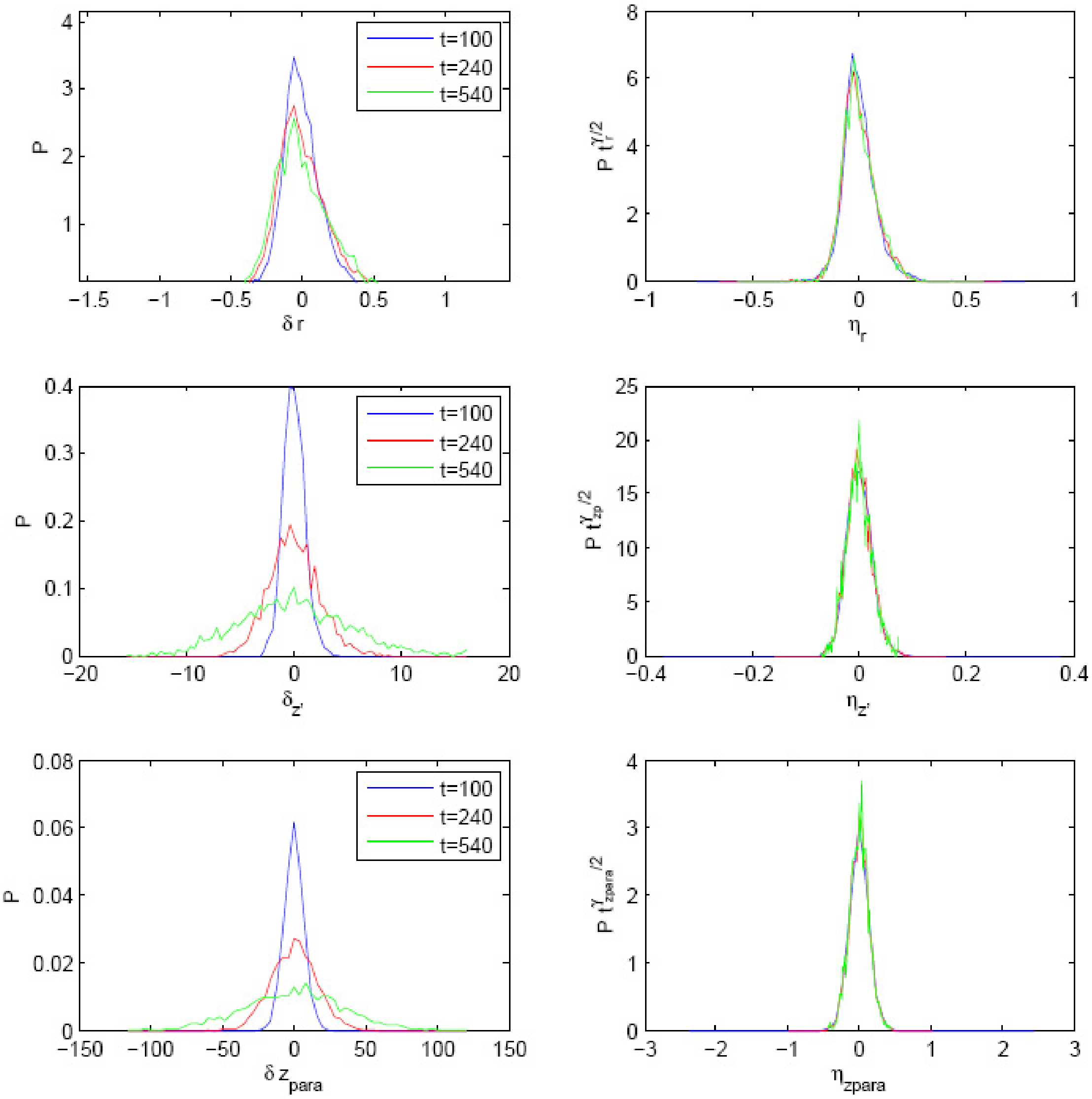

Figure 4.7: Renormalization of the PDF's of particles displacements obtained for three different times, for a simulation at T=0.5=500 eV with N=3'000. $\eta_x = \delta x / t^{\gamma_x/2}$.

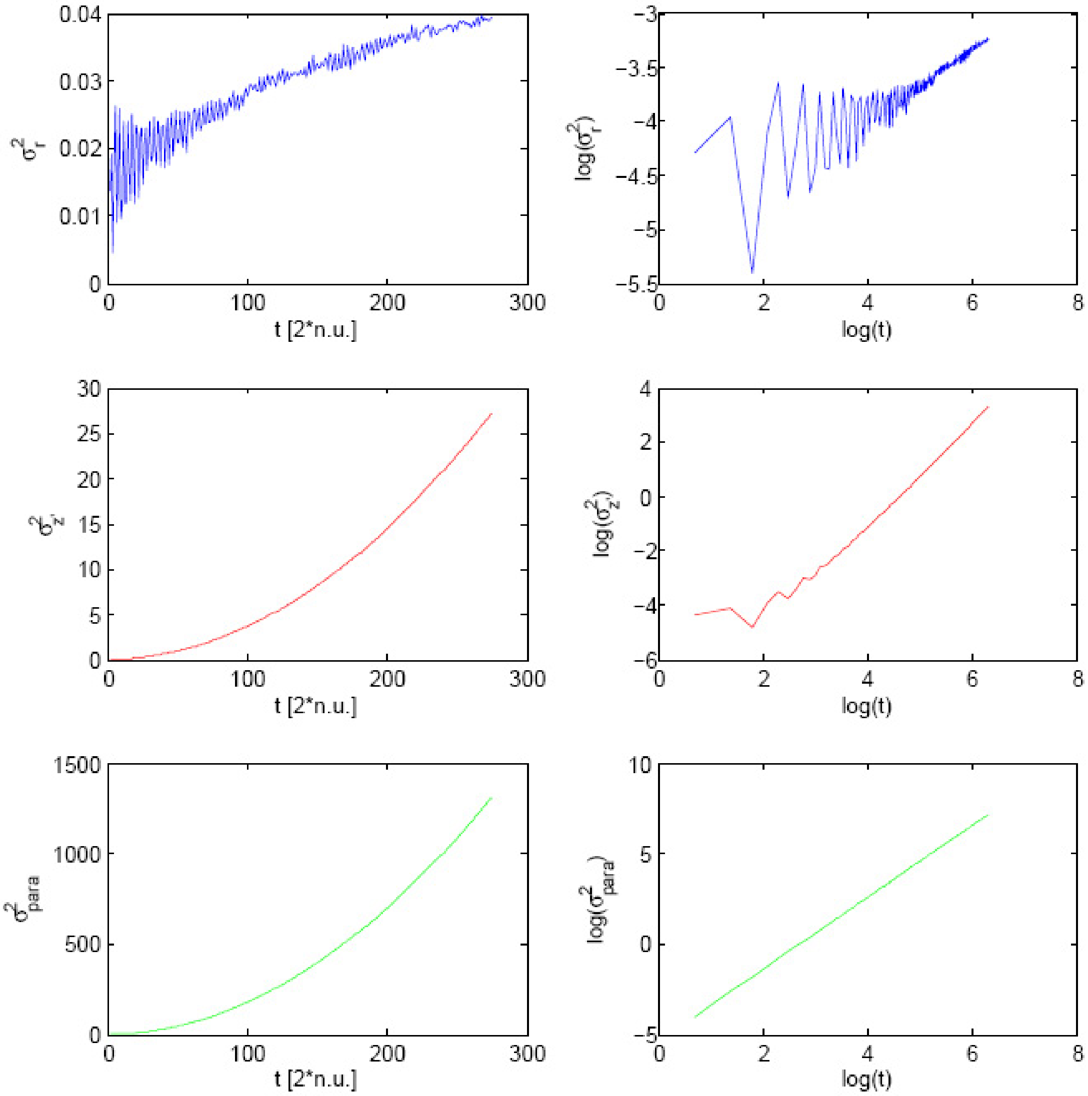

Figure 4.8: Time evolution of the values of σ_i^2, where i=r,z',φ' , in real scale and in log-log scale, for a simulation at T=0.5=500 eV with N=3'000.

function of particles displacements P. Indeed, as seen in section 1.3, this function P has the property that, the plots of $t^{\gamma/2} \cdot P$ vs $\delta y(t)/t^{\gamma/2}$ obtained for different time t should all collapse into the same general function L. And moreover, testing if this property is still valid with exponents $\gamma \pm \delta\gamma$ for different $\delta\gamma$ gives an idea of the correct error $\delta\gamma$ associated to each value of γ. An example of application of this renormalization of the PDF's of particles displacements is presented on the right part of figure 4.7.

4.3.2 Spreading in the case without potential

Before analysing the spreading exponents γ's obtained in simulations where the plasma potential affects the motion of the particles, it can be useful to study a simulation of the simple case where $\phi(t) = 0$, i.e. where the particles are only subject to the magnetic field. The values of γ's coming from this simulation are presented in Table 4.1. The margin of errors are defined as explained in section 4.3.1.

T	N	$\phi(t)$	γ_r	$\gamma_{z'}$	$\gamma_{\parallel}$
0.85	3'000	0	0.0 +0.2	2.0±0.15	2.0±0.15

Table 4.1: Spreading exponents for the three directions, in a simulation with T=0.85=850 eV, without potential, with the source parallel to the magnetic field lines, with a spreading in the initial velocities of $\sigma_{vin}=0.1\cdot\sqrt{T}$, and a spreading in the initial angles of $\sigma_\alpha=0.1$.

Without potential, the motion of a particle depends on the initial velocity of the particle, on the $\bigtriangledown\vec{B}$-drift and on the curvature effect. In the radial direction, the particles move only because of their Larmor rotation, and this rotation is periodic in time. Therefore, σ_r^2 is independent of time, and this explains why $\gamma_r=0$. In the parallel direction, the differences in the motion of the particles are only due to their different initial velocities. Indeed, the $\bigtriangledown\vec{B}$-drift and the curvature effect do not act in the parallel direction. So,

$$\sigma_{\parallel} \propto (v_{\parallel_{max}} - v_{\parallel_{min}}) \cdot t \tag{4.24}$$

This explains why a ballistic spreading is observed in the parallel direction. Finally, the ballistic exponent obtained for the z'-direction can be explained by looking at the definition of $\sigma_{z'}^2$:

$$\begin{aligned}
\sigma_{z'}^2 &= \frac{1}{N}\sum_{i=1}^{N}(z_i(t) - z_{cm_i}(t))^2 && (4.25)\\
&= \frac{1}{N}\sum_{i=1}^{N}(v_{z_i}(t)\cdot t - v_{z,cm_i}(t)\cdot t)^2 && (4.26)\\
&= \frac{t^2}{N}\sum_{i=1}^{N}(v_{z_i}(t) - v_{z,cm_i}(t))^2 && (4.27)
\end{aligned}$$

$$\propto \frac{t^2}{N}\sum_{i=1}^{N}\underbrace{((v_{\|_i}^2(t)+\frac{v_{\perp_i}^2(t)}{2})-v_{z,cm_i}(t))^2}_{U} \tag{4.28}$$

where the last step was to replace the velocity of the particle i by its guiding center velocity. The parallel velocity of a particle i, $v_{\|_i}$, is constant, and, in the particular case without potential, $v_{\perp_i}$ is also constant. Moreover, the z'-velocity of the center of mass is also independent of time, since it is an average on quantities independent on time. Therefore, the term U has no time dependence, and we are left with $\sigma_{z'}^2 \propto t^2$. The spreading is ballistic, as expected. In the presence of $\phi(t) \neq 0$, $v_\perp$ would depend on time, and this reasoning would therefore not be valid.

4.3.3 Spreading exponents for different initial energies

Table 4.2 presents the values of the exponents γ's obtained from simulations with the turbulent potential, for different initial energies of the particles. One can notice that the number of particles required to have a convergence in the σ's increases when the energy of the particles decreases.

T[n.u.]	T[eV]	N	γ_r	$\gamma_{z'}$	$\gamma_\|$
2	2000	3'000	0.26	2.00	1.98
1	1000	3'000	0.34	1.97	1.99
0.85	850	3'000	0.36	1.96	1.99
0.75	750	3'000	0.34	1.95	1.98
0.6	600	3'000	0.31	1.95	1.99
0.5	500	3'000	0.34	1.92	1.99
0.3	300	10'000	0.55	1.74	2.00
0.1	100	10'000	0.65	1.29	2.07
0.05	50	30'000	0.65	1.52	2.13
0.03	30	30'000	0.65	1.54	2.15

Table 4.2: Values of the spreading exponents as a function of the different initial energies of the particles, with realistic potential, with the source parallel to the magnetic field lines, with a spreading in the initial velocities of $\sigma_{v_{in}}$=$0.1\cdot\sqrt{T}$, and a spreading in the initial angles of σ_α=0.1 . The margin of error of these values of γ is about ± 0.15 for all energies and for the three directions.

The first observation is that the parallel spreading is ballistic at any energy. This was expected since, similarly to the case with $\phi(t) = 0$, only the differences in the initial velocities of the different particles of a distribution induce differences in the motion of the particles. Another observation is that, for all energies, γ_r is inferior to 1, and $\gamma_{z'}$ is superior to 1. This means that the transport is always sub-diffusive in this r-direction, and super-diffusive is the z'-direction. Furthermore, one can see that, as the energy increases, γ_r and $\gamma_{z'}$ become closer to their values in the case without potential. This can be explained by the fact that, at high energy, the Larmor radius is big, so the particle rotation averages the effect of the variations of the electric field.

4.3.4 Effect of the spreading in the initial velocities of the particles

Table 4.2 shows that the spreading is ballistic in the parallel direction, for any energy, and in the z'-direction when T is above 0.6=600 eV. These exponents have all been obtained with a spreading in the initial velocities of the particles of $\sigma_{v_{in}} = 0.1 \cdot \sqrt{T}$. It is interesting to study how this ballistic spreading is influenced by a change in $\sigma_{v_{in}}$. The two paragraphs below show that, for the two directions, as long as the spreading is ballistic, σ_i should depend linearly on $\sigma_{v_{in}}$.

Spreading in the parallel direction

Since $v_{\|}$ is conserved along a trajectory, the space between the particles can only come from the difference in their initial velocities. We define $v_{max} = v_0 + \sigma_{vin}$ and $v_{min} = v_0 - \sigma_{vin}$. It follows that:

$$\sigma_{\|} \propto (v_{max} - v_{min})\, t \propto \sigma_{vin}\, t \tag{4.29}$$

Spreading in the z'-direction

The fact that the particles follow different trajectories can be due to the $\vec{E} \times \vec{B}$-drift, the $\bigtriangledown \vec{B}$-drift and the curvature effect. The $\vec{E} \times \vec{B}$-drift does not depend on the difference in the velocities. The combined effect of the $\bigtriangledown \vec{B}$ and the curvature is proportional to $(v_{\|}^2 + \frac{v_{\perp}^2}{2})$. So $v_{z'}$ is propotional to $(v_{\|}^2 + \frac{v_{\perp}^2}{2})$. Moreover, it has been observed that a change of $\sigma_{v_{in}}$ will have an effect on $<v_{\|}^2>$, but not on $<v_{\perp}^2>$, and the term $<v_{\perp}^2>$ is always much smaller than the term $<v_{\|}^2>$ due to the initial inclination of the source. The calculation of the dependence of $\sigma_{z'}$ on $\sigma_{v_{in}}$ is therefore:

$$\begin{aligned}
\sigma_{z'} &\propto (v_{z'max} - v_{z'min})\, t && (4.30)\\
&\propto ((v_{\|max}^2 + \frac{v_{\perp max}^2}{2}) - (v_{\|min}^2 + \frac{v_{\perp min}^2}{2}))\, t && (4.31)\\
&\propto (v_{\|max}^2 - v_{\|min}^2)\, t + \text{const} \cdot t && (4.32)\\
&\propto \underbrace{(v_{\|max} + v_{\|min})}_{2v_0} \underbrace{(v_{\|max} - v_{\|min})}_{\propto \sigma_{vin}}\, t + \text{const} \cdot t && (4.33)\\
&\propto \sigma_{vin}\, t + \text{const} \cdot t && (4.34)
\end{aligned}$$

where the term const $\cdot\, t$ does not depend on $\sigma_{v_{in}}$ and is negligible compared to the term coming from the parallel velocity. Therefore, for ballistic spreading, $\sigma_{z'}$ should depend linearly on $\sigma_{v_{in}}$.

The test of the linear dependence of $\sigma_{\|}$ and $\sigma_{z'}$ on the spreading in the initial velocities is presented in figure 4.9 for simulations at T=0.75. In order to observe only the effect of the initial velocities on the motion of the particles, these plots have been obtained with simulations where all the particles start with the same initial angle. We see that, for any $\sigma_{v_{in}}$ above $\sigma_{v_{in}} = 0.01 \cdot \sqrt{T}$, the relationship is linear, as predicted for a ballistic spreading. However, when $\sigma_{v_{in}} \leq 0.01 \cdot \sqrt{T}$, $\sigma_{\|}$ and $\sigma_{z'}$ do not tend to zero, but reach a constant value. These values reached when $\sigma_{v_{in}} \rightarrow 0$ can be due to two factors. Either they come from the chaotic behavior of the particles trajectories; indeed even a very small change in the initial conditions could create a non-negligible difference in the particles positions after a long time. Or they come from the fact that, in this simulation, every set of 100 particles starts at a very different time. Therefore, the potential under which the particles move is very different for each set of 100 particles. This second effect would induce a non-zero value of $\sigma_{||}$ and $\sigma_{z'}$, even if $\sigma_{v_{in}}$ were equal to zero.

In order to determine which one of these two effects is dominant at $\sigma_{v_{in}} \rightarrow 0$, two simulations have been run. The first one corresponds to a very small difference in the initial velocities of the particles, $\sigma_{v_{in}} = 0.001 \cdot \sqrt{T}$, but where all the particles starts at the exact same time (therefore they all experience the same potential). The goal of this simulation is to isolate the effect of the sensitivity to the initial conditions; it is represented on figure 4.9 by the green point. In the second simulation, all the particles start with exactly the same initial velocity v_0, but they don't experience the same potential, since, as in normal simulations, each set of 100 particles start at a different time. This second simulation corresponds to the blue points of figure 4.9. We can clearly notice that the effect of the sensitivity to the initial conditions is negligible compared to the effect of the difference in the potential. The value of $\sigma_{z'}$ in the first test simulation was so small and fluctuating that it was not possible to evaluate it clearly.

We can therefore conclude that the non-zero value of $\sigma_{||}$ and $\sigma_{z'}$ when $\sigma_{v_{in}} = 0$ is due to the difference in the potential felt by the particles. It has been tested that:

- the values of the blue points change when the intensity of the potential changes.
- the values of the blue points do not depend on the initial energy of the particles.

The above observations tell that the ballistic spreading obtained in the parallel direction and in the z'-direction for most of the energies is an effect of the magnetic field. Thus, the fluctuating electric field only induces a small shift from the ballistic values predicted for $\sigma_{||}$ and $\sigma_{z'}$. This hypothesis has been tested in two other simulations. Indeed, if as assumed here, the effects on $\sigma_{||}$ and $\sigma_{z'}$ of an addition of an electric field in the simulation is only a shift compared to the ballistic values, then changing the intensity of $\phi(t)$ would only increase or decrease the value of this shift. The results of two simulations, one with the intensity of $\phi(t)$ divided by a factor of 10, the other one with the intensity of $\phi(t)$ multiplied by a factor of 10 are presented in the red and yellow points on figure 4.9. As expected, these points are close to the one obtained with the realistic $\phi(t)$. It can particularly be noticed that there is almost no difference between the red points and the points obtained with realistic $\phi(t)$. Moreover, the effect of an increase of the potential is more important in the z'-direction than in the parallel direction. This is normal, since the $\vec{E} \times \vec{B}$-drift acts in the perpendicular plane, but not in the parallel direction. A change of potential has, however, a small effect on the parallel spreading, probably due to an effect of transition from perpendicular velocity to parallel velocity induced by the curvature of $\vec{B}$.

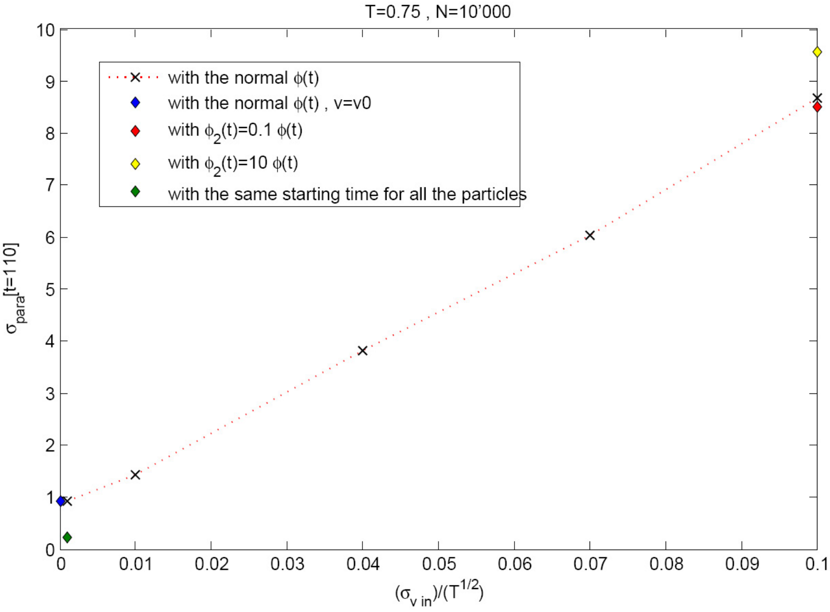

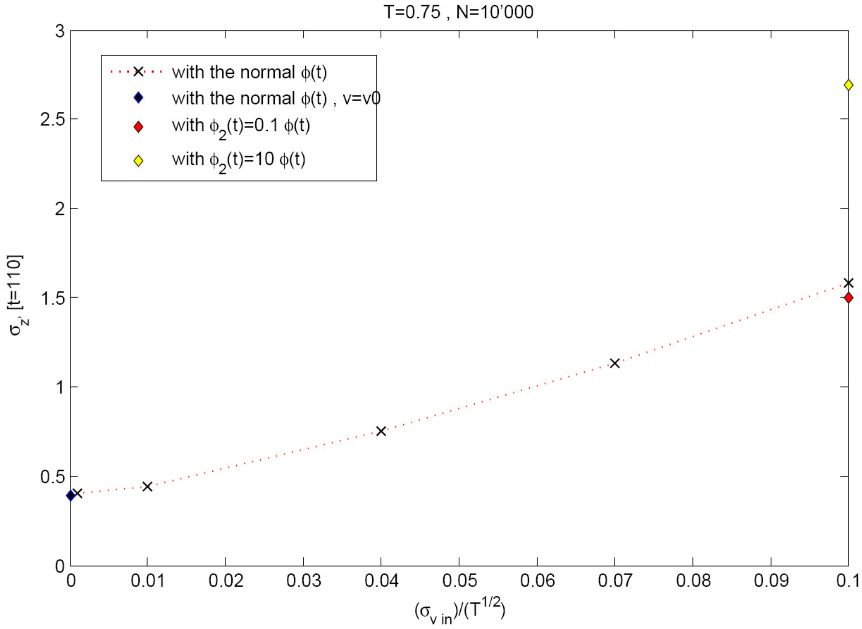

Figure 4.9: Test of the effect of $\sigma_{v_{in}}$ on the spreading in the parallel and in the z'-direction, at T=0.75=750 eV, with $\sigma_\alpha = 0.0$ and $\alpha_0 = \theta$.

T	N	σ_{vin}	$\gamma_{z'}$	$\gamma_{\|\|}$
0.75	10'000	$0.001{\cdot}\sqrt{T}$	1.13	2.43
0.75	10'000	$0.01{\cdot}\sqrt{T}$	1.32	2.14

Table 4.3: Values of the spreading exponents obtained with very small differences in the initial velocities of the particles, with normal potential $\phi(t)$ and with a spreading in the initial angles of σ_α=0.0 . The margin of error is about ± 0.25 for $\gamma_{z'}$, and ± 0.2 for $\gamma_{||}$.

As seen in figure 4.9, the effect of the electric field become dominant only for very small values of $\sigma_{v_{in}}$. Therefore, in the real experiment, if one wants to study the effect of the turbulent potential, the source must induces a very small difference in the initial velocities of the particles. Else, only the ballistic effect of v_{in} will be observed. Table 4.3 presents the values of the exponents γ obtained with the two simulations with the smallest σ_{vin}. The values for $\gamma_{z'}$ are very different from the ballistic exponents obtained with $\sigma_{vin} = 0.1\sqrt{T}$. This tells us that, as expected, the spreading in the z'-direction is not ballistic when the effect of the electric field is dominant.

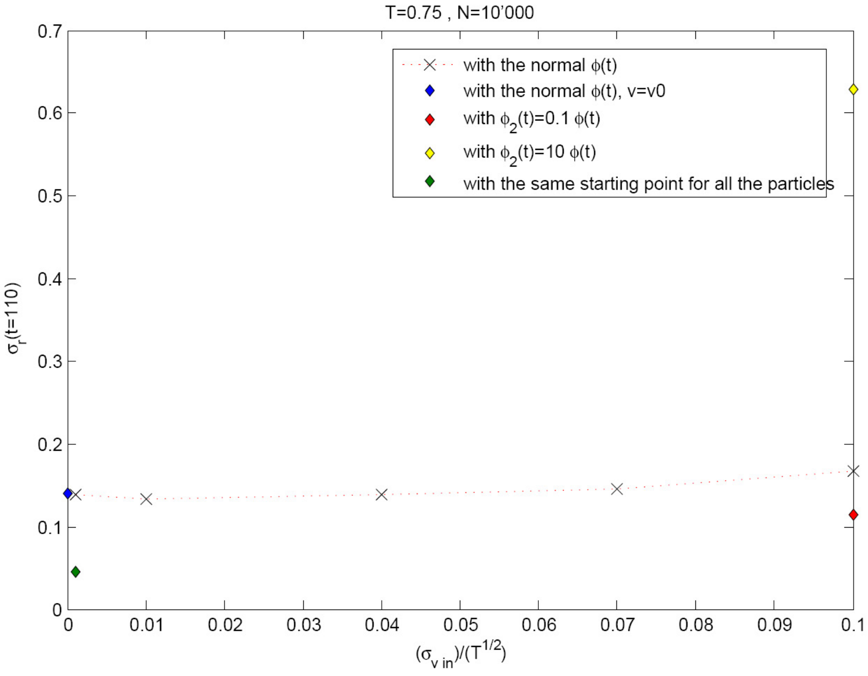

Figure 4.10: Test of the effect of $\sigma_{v_{in}}$ on the spreading in the radial direction, at T=0.75=750 eV, with $\sigma_\alpha = 0.0$ and $\alpha_0 = \theta$.

A similar study of the influence of the spreading in the initial velocities of the particles has been performed for the spreading in the radial direction and is presented in figure 4.10. One can notice on this plot that, unlike in figure 4.9, the radial spreading is almost independent of the differences in the initial velocities. This was expected, since only the $\vec{E} \times \vec{B}$-drift and the Larmor rotation influence the radial motion of the particles; and we have seen that the Larmor rotation does not influence the value of σ_r and the $\vec{E} \times \vec{B}$-drift is not affected by a change in σ_{vin}. The blue point of figure 4.10 tells us that, similarly to the z'- and parallel cases, the non-zero value of σ_r is due to the fact that each set of 100 particles experiences a very different potential. Furthermore, the red and yellow points of figure 4.10 indicate that the radial spreading is much more sensitive to a change in the intensity of the potential than the spreading in the z'- or parallel directions.

4.3.5 Asymmetry in the radial spreading

The radial direction is the direction where the spreading is the most dependent on the electric field. The radial spreading is, therefore, an important element in the study of the effect of turbulence on a distribution of particles. Some elements of analysis of the radial spreading have been realized during this project and are presented below. However, further work on this topic would be necessary in order to reach a deeper understanding of the subject.

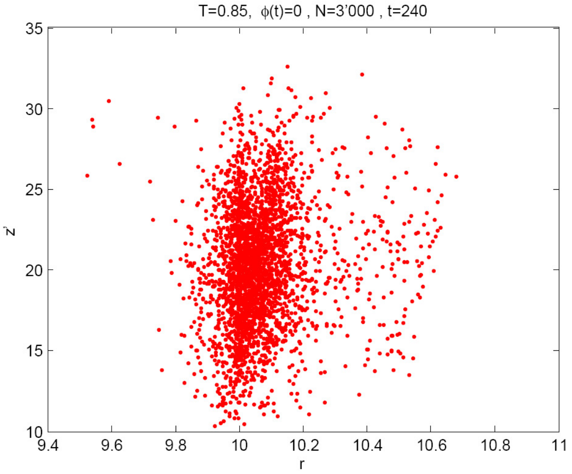

Figure 4.11: Plot of the positions at a given time of a distribution of 3'000 particles in the plane perpendicular to the magnetic field line, for a simulation with T=0.85=850 eV and without potential.

An effect noticed about the spreading in the radial direction is that at high energy (when T≥0.6=600 eV), the distribution of the particles displacements is asymmetric. Indeed it can be observed in figure 4.11 that the density of particles is higher in the high field side region than in the low field side region.

This asymmetry appears after a very short time, and it is not an effect of the potential. Indeed, figure 4.12 shows the PDF's of particles displacements at different times for two simulations with the same initial energy; one taking into account the

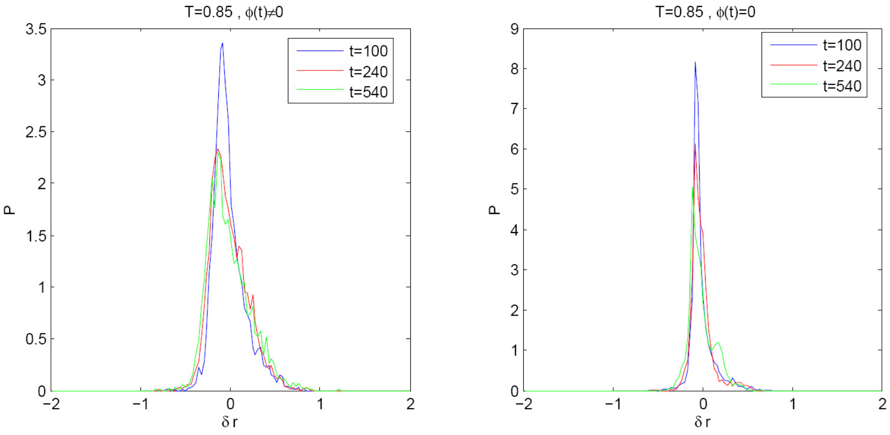

Figure 4.12: PDF's of particles radial displacements, in the cases with and without potential, with the same energy T=0.85=850 eV .

simulated potential, and one without potential. Since the asymmetry appears in both distributions, it must be an effect of the magnetic field.

It have been seen in section 3.1.1 that the Larmor radius of a particle depends on the angle between its initial velocity and the magnetic field line. If this angle is bigger than zero, then the particle rotates toward the high field side and its Larmor radius is smaller than if its initial angle is negative, in which case the particle rotates toward the low field side. Therefore, the particles in the low field side region of the vacuum vessel rotate with a bigger Larmor radius, and this explains why the particle density is smaller there and why the distributions of figure 4.12 are asymmetric. Figure 4.13 presents the distribution of the initial angles of all the particles of the simulation corresponding to the right part of figure 4.12. If this explanation of the asymmetry is correct, then the particles corresponding to the tail of the radial distributions (toward the low field side) must have a negative initial angle. On figure 4.13, the red points correspond to the particles belonging to the tail of the distributions ($\delta r > 0.5$) at a given time. We see that the initial angle of all the red particles have a high negative value, which validates this explanation.

This asymmetry does not occur for energies below T=0.6=600eV, probably because, in these cases, the differences in the Larmor radius of the particles is too small to be noticed. This phenomena is, of course, independent of the electric field, and it has to be taken into account in the experimental study of the effect of the turbulent potential on the fast ions.

4.3.6 Influence of the spreading in the initial angles

Another parameter that affects the spreading of a distribution of particles is the difference in the initial angles of the particles velocities. Table 4.4 presents the effect of a variation of the spreading in the initial angles on the exponents γ.

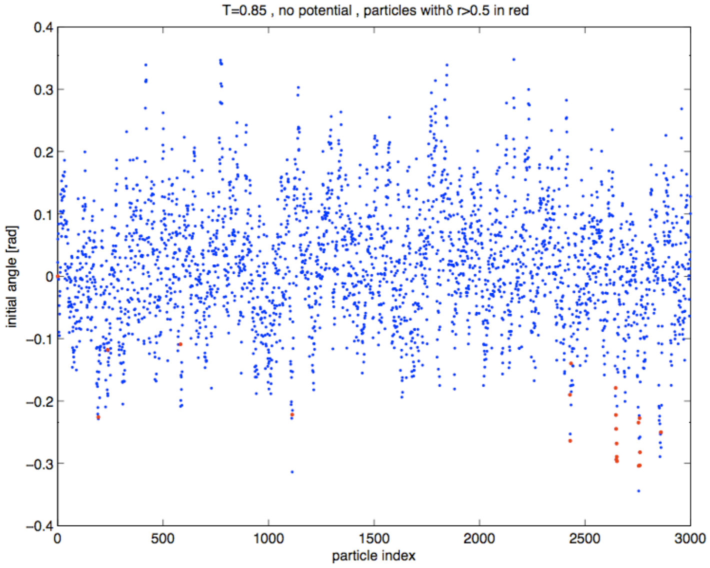

Figure 4.13: Initial angles of all the particles of a the simulation corresponding to the right part of figure 4.12. The particles in red are the one belonging to the tail of the radial distributions ($\delta r > 0.5$).

σ_α	$\sigma_\alpha[^\circ]$	γ_r	$\gamma_{z'}$	$\gamma_{\|}$
0.01	0.57 °	0.42	1.98	1.98
0.1	5.73 °	0.34	1.95	1.98
0.2	11.46 °	0.20	1.95	1.99
0.3	17.19 °	0.12	1.94	2.00
0.4	22.92 °	0.00	1.90	2.00

Table 4.4: Effect of a variation of spreading in the initial angles on the exponents γ, for a distribution of 3'000 particles, with T=0.75=750 eV and with a spreading in the initial velocities of $\sigma_{vin} = 0.1 \cdot \sqrt{T}$. The margin of error is about ± 0.15 for the three directions.

As expected, the parallel and z' spreading are not very affected by the variations of σ_α. Indeed, the exponents reveal a ballistic dynamics. We notice thus a small decrease in the values of the $\gamma_{z'}$. The bigger effect of the variations of σ_α is visible on the radial exponents. Indeed, the values of γ_r tends to 0 as the spreading in the initial angles increases. Since $\gamma_r = 0$ correspond to the simulation without potential, we can assume that the decrease of γ_r is due to the fact that, as the initial angles increase, the Larmor radii of the particles toward the sides of the angles distribution increase. And it has been seen that, a big Larmor rotation has an effect of averaging the variations of potential.

Conclusion

The fast ions experiment on the TORPEX device at the CRPP institute in Lausanne, is built with the goal of helping our understanding of the interactions between fast ions and a low-frequency turbulent plasma. Implementing a simulation of this experiment can be a useful tool to predict and analyze the results of this fast ions experiment.

While the motion of a single particle in a magnetic field has already been implemented and tested during the tp4-project, the first part of this master project has been the implementation and test of the motion of a single particle in the electric field coming from a simulated turbulent potential, the implementation of the time dependence of the potential, and the implementation of the motion of a statistically meaningful number of particles.

The study of the effect of the magnetic field, the variation in space of the electric field, and the time dependence of the electric field on the trajectory of a single particle, has given results that follow the theoretical expectations, confirming that the solver is implemented correctly. Furthermore, a chaotic behavior has been observed for a single particle motion, particularly a high sensitivity to the initial conditions. The comparison of a single particle trajectory with the guiding center equations has shown that the guiding center model gives a good approximation of the particle trajectory, for all the energies considered, when the source is parallel to the magnetic field lines. The use of the guiding center equations to estimate the velocity of the center of mass has given very positive results. It has been seen that the effect of turbulence is not observable by studying the motion of the center of mass. However an effect of the time average of the electric field can be observed. An approximation is given for the trajectory of the center of mass when the source is parallel to the magnetic field lines. It can be useful as a prediction for the experiment. Finally, the study of the spreading in the parallel direction and in the perpendicular plane has shown that:

- In simulations without potential, the spreading is ballistic in the z'- and in the parallel direction, and the beam remains focused in the radial direction.
- At high energy and big initial spreading, the exponents γ's come closer to their values in simulations without potential. Therefore, the effect of the turbulent potential on the distributions become negligible as the energy increases.
- The spreading in the parallel direction and in the z'-direction at high energy ($T \geq 600$ eV) is ballistic and depends linearly on the spreading in the initial

velocities.

- The effect of the electric field on the parallel and z' spreading become important only when the spreading in the initial velocities is very small ($\sigma_{v_{in}} \leq 0.01 \cdot \sqrt{T}$).
- The dependence of the radial spreading on the electric field, is stronger than the dependence of the spreading in the other directions. Therefore, the radial spreading can be a key element in the study of the effect of turbulence on a distribution of fast ions.
- The radial distributions exhibit an asymmetry toward the low field side. This asymmetry is an effect of the r dependence of the toroidal magnetic field.
- The effect of the turbulent potential decreases as the variance of the initial angles increases.

Therefore, the effect of turbulence are visible in the radial dynamics, in the parallel and z' dynamics if $\sigma_{v_{in}} \leq 0.01 \cdot \sqrt{T}$, for small initial angles.

To conclude, let me give an outlook of the further work that could be realized. The first thing to do is to study in more details the spreading in the radial direction. Then, an aspect that has not been studied during this project is the effect of the inclination of the source on the spreading of the particles. Indeed, the study of the effect of the spreading in the initial angles showed that the initial angles of the particles could be an important point. Another possible study is the effect of the position of the source in the poloidal cross section. It also would be very interesting to compare the dynamics of fast ions in different turbulent regimes [15]. On a more theoretical level, since non-diffusive transport has been observed, it would be interesting to study the non-diffusive transport theory and try to apply the equations for transport using fractional derivatives to the results of the simulation, which would require to obtain an estimation for the fractional numbers α and β that appear in the generalized diffusion equation. Finally, in order to increase the similarity of the simulation with the real experiment, the next step would be to add to the code the collisions between fast ions and the background plasma and the neutrals.

Appendix A

Mathematical appendix

A.1 The bicubic interpolation method

The bicubic interpolation (well described in [12]) is the method used in this project to obtain the values of the potential $\phi(t)$, from some tabulated values on a grid. This method has the property to create an interpolated function that is continuous, with gradient also continuous. This property was indeed required in the project, since the particles motions are influenced by the electric field, which is the gradient of the potential. A second property of this method is that the values of the function y and the specified derivatives, at the grid points, are exactly equal to the discretized values given as inputs.

In order to find the value of the function $y(x_1, x_2)$ where x_1 and x_2 can be any point in the 2D plane, the bicubic interpolation requires the knowledge of the values of the function y at each grid points (called y_d), but also the values of the gradients $\partial y/\partial x_1 \equiv y_{,1}$, $\partial y/\partial x_2 \equiv y_{,2}$ and the cross derivative: $\partial^2 y/\partial x_1 \partial x_2 \equiv y_{,12}$. In this project, these derivatives have been obtained by numerical differentiation from the values of y_d already tabulated for the grid points.

The indices j and k define the grid square that contains the point (x_1, x_2).

$$x1_d[j] \leq \quad x_1 \quad \leq x1_d[j+1] \tag{A.1}$$

$$x2_d[k] \leq \quad x_2 \quad \leq x2_d[k+1] \tag{A.2}$$

And the position inside the gris square is given by the values of t and u (t,u $\in$[0;1]), defined as:

$$t = (x_1 - x1_d[j])/d_1 \tag{A.3}$$

$$u = (x_2 - x2_d[k])/d_2 \tag{A.4}$$

where $d_1 = (x1_d[j+1] - x1_d[j])$ and $d_2 = (x2_d[k+1] - x2_d[k])$ are the length of the grid cell in the 2 directions.

The equations that give the values of the function, gradients and cross derivative from the discretized values of the function and derivatives are:

$$\begin{aligned}
y(x_1,x_2) &= \sum_{i=0}^{3}\sum_{j=0}^{3} c_{ij} t^i u^j && \text{(A.5)}\\
y_{,1}(x_1,x_2) &= \sum_{i=0}^{3}\sum_{j=0}^{3} i\, c_{ij} t^{i-1} u^j (\frac{dt}{dx_1}) && \text{(A.6)}\\
y_{,2}(x_1,x_2) &= \sum_{i=0}^{3}\sum_{j=0}^{3} j\, c_{ij} t^i u^{j-1} (\frac{du}{dx_2}) && \text{(A.7)}\\
y_{,12}(x_1,x_2) &= \sum_{i=0}^{3}\sum_{j=0}^{3} i\, j\, c_{ij} t^{i-1} u^{j-1} (\frac{dt}{dx_1})(\frac{du}{dx_2}) && \text{(A.8)}
\end{aligned}$$

The coefficients c_{ij} are obtained by linear transformations. To preform the calculation of those coefficients, we define the vectors:

- y[0..3] are the values of the function y at the four points of the grid cell, numbered counterclockwise from the lower left.
- y1[0..3], y2[0..3], y12[0..3] the values of the gradients and cross derivative at those points.

The vector $\mathcal{X}$ is then defined as:

$$\mathcal{X} = \begin{pmatrix} y[0] \\ y[1] \\ y[2] \\ y[3] \\ y1[0]\cdot d_1 \\ y1[1]\cdot d_1 \\ y1[2]\cdot d_1 \\ y1[3]\cdot d_1 \\ y2[0]\cdot d_2 \\ y2[1]\cdot d_2 \\ y2[2]\cdot d_2 \\ y2[3]\cdot d_2 \\ y12[0]\cdot d_1\cdot d_2 \\ y12[1]\cdot d_1\cdot d_2 \\ y12[2]\cdot d_1\cdot d_2 \\ y12[3]\cdot d_1\cdot d_2 \end{pmatrix}$$

The multiplication of the vector $\mathcal{X}$ by the matrix $\mathcal{M}$ gives a vector $\mathcal{C}$ that corresponds to the 16 coefficients c_{ij}.

$$\mathcal{C}^T = (c_{00}, c_{01}, c_{02}, c_{03}, c_{10}, c_{12}, ..., c_{33}) \tag{A.9}$$

$$\mathcal{C} = \mathcal{X}\cdot\mathcal{M} \tag{A.10}$$

where M is just a matrix of coefficients:

$$\mathcal{M} = \begin{pmatrix}
1 & 0 & 0 & 0 & 0 & 0 & 0 & 0 & 0 & 0 & 0 & 0 & 0 & 0 & 0 & 0 \\
0 & 0 & 0 & 0 & 0 & 0 & 0 & 0 & 1 & 0 & 0 & 0 & 0 & 0 & 0 & 0 \\
-3 & 0 & 0 & 3 & 0 & 0 & 0 & 0 & -2 & 0 & 0 & -1 & 0 & 0 & 0 & 0 \\
2 & 0 & 0 & -2 & 0 & 0 & 0 & 0 & 1 & 0 & 0 & 1 & 0 & 0 & 0 & 0 \\
0 & 0 & 0 & 0 & 1 & 0 & 0 & 0 & 0 & 0 & 0 & 0 & 0 & 0 & 0 & 0 \\
0 & 0 & 0 & 0 & 0 & 0 & 0 & 0 & 0 & 0 & 0 & 0 & 1 & 0 & 0 & 0 \\
0 & 0 & 0 & 0 & -3 & 0 & 0 & 3 & 0 & 0 & 0 & 0 & -2 & 0 & 0 & -1 \\
0 & 0 & 0 & 0 & 2 & 0 & 0 & -2 & 0 & 0 & 0 & 0 & 1 & 0 & 0 & 1 \\
-3 & 3 & 0 & 0 & -2 & -1 & 0 & 0 & 0 & 0 & 0 & 0 & 0 & 0 & 0 & 0 \\
0 & 0 & 0 & 0 & 0 & 0 & 0 & 0 & -3 & 3 & 0 & 0 & -2 & -1 & 0 & 0 \\
9 & -9 & 9 & -9 & 6 & 3 & -3 & -6 & 6 & -6 & -3 & 3 & 4 & 2 & 1 & 2 \\
-6 & 6 & -6 & 6 & -4 & -2 & 2 & 4 & -3 & 3 & 3 & -3 & -2 & -1 & -1 & -2 \\
2 & -2 & 0 & 0 & 1 & 1 & 0 & 0 & 0 & 0 & 0 & 0 & 0 & 0 & 0 & 0 \\
0 & 0 & 0 & 0 & 0 & 0 & 0 & 0 & 2 & -2 & 0 & 0 & 1 & 1 & 0 & 0 \\
-6 & 6 & -6 & 6 & -3 & -3 & 3 & 3 & -4 & 4 & 2 & -2 & -2 & -2 & -1 & -1 \\
4 & -4 & 4 & -4 & 2 & 2 & -2 & -2 & 2 & -2 & -2 & 2 & 1 & 1 & 1 & 1
\end{pmatrix}$$

A.2 Definition of the correlation function

The correlation function of a signal u(t) is, mathematically, the cross-correlation of this signal with itself but at a later time. If τ is the time interval, the definition of the correlation factor $c(\tau)$ is given by:

$$c(\tau) = \frac{< u(t)\, u(t+\tau) >_t - < u(t) >_t < u(t+\tau) >_t}{\sqrt{< (u(t) - < u(t) >_t)^2 >_t < (u(t+\tau) - < u(t+\tau) >_t)^2 >_t}} \tag{A.11}$$

$c(\tau)$ can take values between -1 and 1; 1 representing perfect correlation, and -1 representing perfect anti-correlation.

For any signals, $c(\tau = 0) = 1$ and $c(\tau) \leq c(0) \forall \tau$.

Appendix B

Metropolis algorithm for the creation of a weighted distribution

The Metropolis algorithm is used to generate a chain of random numbers, where the distribution of these numbers follow a certain probability function called the weight of the distribution w(x). In the problem of approximating a gaussian distribution, with σ and x_0 given, the weight is given by the equation:

$$w(x) = \frac{1}{\sigma\sqrt{2\pi}} e^{-\frac{(x-x_0)^2}{2\sigma^2}} \tag{B.1}$$

The Metropolis algorithm generates a Markov chain where the element x^{n+1} depends only on x^n. The algorithm is the following:

1. A number x' is proposed as a possible value for the step n+1. It is computed from x^n, following:
$$x' = x^n \pm \delta \cdot r_1 \tag{B.2}$$
where r_1 is a random number, $r_1 \in$[0;1].

2. Then the value x' is accepted, or not, depending on its weight. We define a as:
$$a = \frac{w(x')}{w(x^n)} \tag{B.3}$$
If a>1, x' is accepted as the value for the step n+1 (x^{n+1}=x').

3. If a<1, x' has still a probability to be accepted equal to a. To compute this probability, the program generates a new random number $r_2 \in$[0;1]. If $a > r_2$, then x' is accepted (x^{n+1}=x'). If $a < r_2$, x' is rejected and the program goes back to step 1.

An important quantity that defines the precision of the Metropolis algorithm is the acceptance rate of the x' s. It depends directly on the value of δ. In an good algorithm, δ should be chosen in order to obtain an acceptance rate of 50%.

Bibliography

[1] *Plasma physics via computer simulation*, C. K. Bidsall and A. B. Langdon, *McGraw-Hill book company*, 1985.

[2] *Waves and Instabilities in Inhomogeneous Plasmas*, S. Brunner, 3rd cycle course, EPFL

[3] *Non diffusive transport in fusion plasmas: a fractional diffusion approach* D. del-Castillo-Negrete, *1rst ITER Summer School*, Aix en Provence, France, July 2007

[4] *Finite Larmor radius effects on non-diffusive tracer transport in a zonal flow*, K. Gustafson, D. del-Castillo-Negrete, W. Dorland

[5] *Etude experimentale des modes de confinement L et H dans un plasma toroidal simplement magnetise*, Guterl Jerome, Projet de tp4 sous la direction d'Ivo Furno, juin 2008

[6] *Theory of plasma transport in toroidal confinement systems*, F. L. Hinton and R. D. Hazeltine, *Reviews of modern physics, vol. 48, Issue 2, Pages 239-308*, 1976.

[7] *Principles of plasma physics*, N. A. Krall and A. W. Trivelpiec, *McGraw-Hill book company*, 1973.

[8] *Phenomenes non-lineaires et chaos* H. Kunz, Master course, EPFL

[9] *NRL Plasma Formulary*, Naval Research Laboratory, Washington DC, Revised 2000

[10] *ITER Physics Basis 1999* Nucl. Fusion 39 *Chapter 1*: Overview and summary, *Chapter 5*: Physics of energetic ions

[11] *ITER Physics Basis 2007* Nucl. Fusion 47 *Chapter 5*: Physics of energetic ions

[12] *Fast ion source and detector for investigating the interaction of turbulence with suprathermal ions in a low temperature toroidal plasma*, G. Plyushchev et al, *Review of scientific instruments 77* 2006

[13] *Numerical Recipes: The art of scientific computing*, W. H. Press, S. A. Teukolsky, W. T. Vetterling, B. P. Flannery, 3rd Edition

[14] *High- and Low-Confinement Modes in Simple Magnetized Toroidal Plasmas*, P. Ricci et al, *Physical Review Letters*, 2008

[15] *Langmuir probe-based observables for plasma-turbulence code validation and application to the TORPEX basic plasma physics experiment*, P. Ricci, C. Theiler, A. Fasoli, I. Furno, B. Labit, S.H. Muller, M. Podesta, F.M. Poli, *submitted to Physics of Plasmas*